Eng. Sci., 2025, **38**, 1887

Engineered Science

DOI: https://dx.doi.org/10.30919/es1887

Nickel-Zinc Hydroxide-Orchestrated Nitrogen-Doped Carbon/ Bismuth Vanadate Nanosheet Aerogels Power 24 Hour Solar-to-Hydrogen Systems

Ruhua Zha,[1] Zhen Zhang,[1] Yang Zhang,[1] QingCheng Wang,[1] Liu He,[2] Tuo Shi[3] and Min Zhang[1,*]

Abstract

Ring-opening polymerization (ROP) affords a powerful driving force for the large-scale assembly of polymer precursors and photo-induced charge channels via incorporating aromatic repeat units into the polymer main chain. Herein, a range of monolithic aerogels were constructed based on the polymerization of a branched benzoxazine monomer, in which few-layer $BiVO_4$ nanosheets were embedded within nitrogen self-doped carbon aerogels (NC). The resultant hierarchically structured NC/$BiVO_4$ aerogels exhibited high specific surface area, ultralow density, and high electrical conductivity. The polymerization of the branched benzoxazine monomer facilitated direct and tight contact between NC and $BiVO_4$, contributing to the generation of structural disorder (as evidenced by ^{19}F $\Delta\delta$ and X-ray Pair Distribution Function (PDF) analysis) and thus enabling more efficient storage of reactive ions in the photocatalytic system. As a proof-of-concept demonstration, we assembled an integrated system where solar cells incorporating the 3D monolithic NC/$BiVO_4$ aerogels charged rechargeable Ni-Zn batteries utilizing a zinc-doped nickel-based cathode ($Ni_{0.95}Zn_{0.05}(OH)_{2.0}$), achieving a stable output voltage of 1.89 V. The solar-charged batteries enabled the system to operate not only during the day (via direct solar power) but also at night (via energy released from the batteries), resulting in a 24 h continuous, fully solar-powered uninterrupted overall water-splitting system.

Keywords: Ring-opening polymerization; Nitrogen self-doped carbon aerogels; $BiVO_4$ nanosheets; Structural disorder; Ultrahigh photoreactivity.

Received: 09 August 2025; Revised: 24 October 2025; Accepted: 21 November 2025

Article type: Research article.

1. Introduction

Solar energy that shines upon the earth is thousands of times higher than the energy currently consumed by humanity, thereby furnishing a dependable energy foundation for the long-term utilization of sunlight-driven catalytic reactions.[1,2] With in-depth research on solar energy, researchers have gradually recognized that solar energy cannot only be directly transformed into chemical energy through photocatalytic processes, but can also be transformed into thermal energy and electrical energy to initiate different kinds of catalytic reactions. Solar cells play a crucial role in the electrification of energy demand as well as promoting the share of solar energy for electricity production.[3-5] Water splitting is a fast and cost-effective strategy for converting and storing intermittent solar or electric energy in the form of hydrogen and oxygen chemicalfuels.[6-8] Sole photocatalytic water splitting has great limitations due to the intermittent nature of sunlight, while sole electrocatalytic reaction inevitably uses electricity derived from the power grid, leading to high costs and environmental pollution.[9,10] Therefore, the design and development of fully solar-powered uninterrupted overall water-splitting systems for hydrogen generation are highly desirable yet greatly challenging.

Photocatalytic reactions have a high dependence on light and usually require light of specific wavelengths to activate the catalysts. The proportion of the part that can be effectively utilized by photocatalysts is relatively small, resulting in a low utilization rate of solar energy. Particular catalysts show high catalytic activities for the hydrogen evolution reaction (HER) and oxygen evolution reaction (OER) for water splitting at a high-driving voltage of 1.8-2.0 V, which is much higher than

---

[1] *School of Chemistry and Materials Engineering, Fuyang Normal University, Fuyang, Anhui, 236037, China*

[2] *Department of Medicinal Chemistry, Virginia Commonwealth University, Richmond, Virginia, USA*

[3] *Key Laboratory of Microelectronic Devices and Integrated Technology, Institute of Microelectronics, Chinese Academy of Sciences, Beijing, 100029, China*

[*] *Email:* zm201177055@sina.com (Min Zhang)

the minimal thermodynamic water-splitting potential of 1.23 V.[11] Monoclinic $BiVO_4$ has increasingly become one of the leading actors for photocatalytic water splitting owing to its narrow band gap (2.4 eV), high thermal stability and good photocatalytic capability for H_2 evolution.[12-15] However, the practical application of pure $BiVO_4$ is still dissatisfactory due to the poor transport and the easy recombination of the photoinduced carriers.[16,17] Moreover, the powdered $BiVO_4$ nanoparticles inevitably tend to agglomerate, not only in the preparation process of $BiVO_4$ photocatalyst, but also in the eventual repeated recycling treatment. Monolithic aerogel photocatalysts, a new booming style nicknamed the "solid air", have stood out in photochemical synthesis and green energy production industry.[18,19] The distinctive characteristics of monolithic aerogels include chemical inertness, ultra-light weight (< 0.2 g cm^{-3}), high specific surface area (500-1500 m^2 g^{-1}), high-porosity (> 90% v/v), high macroscopic operability and recoverability.[20] The appearance of monolithic aerogels has stimulated the development of vast numbers of mechanically stable and multi-functional photocatalytic materials at an industrial scale. High-voltage batteries can effectively drive overall water splitting.

When there is no light at night or insufficient indoor lighting, photocatalytic reactions will be greatly limited. Luckily, Ni-Zn batteries can just make up for this shortcoming, and the photocatalytic reaction can be replaced easily to keep the HER and OER processes going.[21-23] As a feasible energy supply, Ni-Zn batteries play a highly important role in electrocatalysis for overall water splitting due to their high output voltage of≈1.75 V and long-term safety. However, the main bottleneck in the development of Ni-Zn batteries for this purposeis low specific capacity due to the lack of a high-performance Ni-based cathode, making self-driven water-splitting devices difficult to achieve.[24,25]

In this work, we demonstrate an integrated system where a solar cell powers water splitting during the day and simultaneously charges a Ni-Zn battery. The stored energy in the battery then powers the water splitting at night, enabling truly uninterrupted 24-hour operation. Large-scale monolithic aerogels derived from phenolic resin were prepared based on the ring-opening polymerization of a branched benzoxazine monomer, in which layered $BiVO_4$ nanosheets was embedded with nitrogen self-doped carbon aerogels (NC). The resultant hierarchically porous NC/$BiVO_4$ aerogels had high specific surface area (758.54-929.21 m^2 g^{-1}), ultralow density (0.13-0.27 g cm^{-3}) and high electrical conductivity (31-58 S cm^{-1}). The polymerization of three functional benzoxazine monomer and the gelation of polybenzoxazine in DMF allowed for direct and tight contact of NC and $BiVO_4$, contributing to the structural disorder of the hybrids. NC/$BiVO_4$ decorated Ni-Zn alkaline batteries. Crucially, ultra-dense NC/$BiVO_4$-coated Co-free Ni-based aerogel cathodes were assembled for practical Ni-Zn batteries with solar passivated emitter and rear cell (PERC) to achieve fully solar self-driven overall water splitting, which demonstrated day and night (24 h) HER and OER without interruptions or degradation. As the sustainable energy input, the role of PERC is to charge the rechargeable Ni-Zn batteries for energy storage so as to provide a steady voltage for electrocatalysis during the night. Hence, this work reforms the traditional photocatalytic reactions, representing an important step in the sustainable development of green and renewable energy management.

2. Experimental

2.1 Materials

4,4,4-(Ethylidene)trisphenol (A.R.), $Bi(NO_3)_3{\cdot}5H_2O$ (A.R.), toluene (A.R.), phenylamine (A.R.), NH_4VO_3 (A.R.), N,N-dimethylformamide (DMF), chloroform (A.R.), sodium hydroxide (A.R.), $Co(NO_3)_2{\cdot}6H_2O$ (A.R.), paraformaldehyde (95%), hydrochloric acid and dichloromethane (A.R.) were purchased from Sinopharm Chemical Reagent Co., Ltd, China. All the pharmaceuticals and solvents were used as received without further purification.

2.2 Fabrication of monomers and aerogels

2.2.1 Synthesis of tri-functional benzoxazine monomer

The benzoxazine monomer was prepared by Mannich reaction.[26] Toluene (100 mL), aniline (2.73 g, 0.03 mol), paraformaldehyde (1.98 g, 0.066 mol), and 1,1,1-tris(4-hydroxyphenyl) ethane (3.0 g, 0.01 mol) were added to a three-necked flask. The flask was placed in an ice bath and the mixture was magnetically stirred for 0.5 h. Then the flask was transferred to an oil bath and the oil was heated to 110 °C. The mixture was continuously refluxed until no water was expelled by azeotropic distillation. The resultant solution was poured into a single-necked flask. The solvent in the solution was removed by rotary evaporation. The residue was purified by extraction using chloroform as the extraction agent. The NaOH aqueous solution (0.1 M) was used to remove the excess paraformaldehyde. Finally, the organic phase was dried with anhydrous Na_2SO_4 (3.00 g). The product (tri-functional benzoxazine monomer TBOZ) was obtained after successively the filtration (to remove anhydrous Na_2SO_4), the rotary evaporation (to remove chloroform) and drying under vacuum at 50 °C for 36 h.

2.2.2 Synthesis of few-layer $BiVO_4$ nanosheets

Into a 100 mL beaker were added 5.0 g $Bi(NO_3)_3{\cdot}5H_2O$, 5 mL oleic acid (OA) and 5 mL oleylamine (OLA) under vigorous stirring to form a homogeneous solution A. Into another 100 mL beaker were added 4.90 g vanadyl acetylacetonate and 10 mL acetylacetone under vigorous stirring to form a homogeneous solution B. Then the solution A was poured into the solution B under vigorous stirring to form a mixed solution with the Bi/V molar ratio of 1/1. The obtained mixture was transferred into a 100 mL teflon-lined stainless steel autoclave, and kept in an oven at 200 °C for 3 h. After the reaction, the autoclave was cooled to room temperature. The resultant raw product was purified by centrifugation at 10,000 rpm for 20 min, washed with water (5 mL), and ethanol (5 mL) three times, then dried at 100 °C for 4 h. The pristine $BiVO_4$ nanoparticles were collected. Finally, into a 100 mL beaker were added 1.0 g of the above $BiVO_4$ nanoparticles and 60 mL acetone under ultrasonic vibration to form homogeneous $BiVO_4$ colloids. The homogeneous $BiVO_4$ colloids were then subjected to freeze drying at -80 °C for 24 h to obtain the dried $BiVO_4$ nanosheet powder**.**

2.2.3 Synthesis of $Ni_{0.95}Zn_{0.05}(OH)_{2.0}$

Typically, into a flask were added $NiSO_4·6H_2O$ (0.95 mol), $ZnSO_4·6H_2O$ (0.05 mol) and Milli-Q water (>18 MΩ cm) to form a solution of 1.0 M. The mixed solution was placed in an oscillating shaker to ensure good mixing. Then NaOH (1.0 M) and NH_4OH (0.25 M) were added as the chelating agents separately and dropwise gradually into the above solution. The reaction proceeded smoothly at 60 °C for 8 h under normal pressure. After the coprecipitation reaction, the powders were filtered and washed with Milli-Q water several times to remove impurities. After dried at 80 °C for 12 h, $Ni_{0.95}Zn_{0.05}(OH)_{2.0}$ nanoparticles were collected.

2.2.4 Synthesis of NC/$BiVO_4$ aerogels

The synthesis of NC/$BiVO_4$ aerogels involved a sol-gel process followed by pyrolysis. Briefly, the TBOZ monomer (carbon and nitrogen source) and $BiVO_4$ nanosheets were co-dispersed in DMF with acetic acid as a catalyst. Upon heating, the ring-opening polymerization of TBOZ occurred, forming a polybenzoxazine gel network that encapsulated the $BiVO_4$ nanosheets. The resulting wet gel was aged, supercritically dried, and finally carbonized to convert the polymer into nitrogen-doped carbon, yielding the monolithic NC/$BiVO_4$ aerogel. The polymerization of TBOZ (PBZ), the gelation and the aging of the hybrids were involved in the synthesis of NC/$BiVO_4$ aerogels. Into a flask A were added TBOZ (3 g) and DMF (30 mL). Into a flask B were added the pristine $BiVO_4$ nanosheets (3 g), acetic acid (10 mL) and DMF (30 mL). The mixture in flask A was mixed with the mixture in flask B. Then the resulting mixture was poured into a tinfoil mold. The tinfoil mold was transferred into a vacuum drying oven to conduct the gelation process (120 °C, 120 min) and the aging process (120 °C, 120 min). Subsequently, the residue in the tinfoil mold was washed with DMF and acetone, respectively, and dried by supercritical drying, leading to the formation of the wet gels. Finally, the temperature programmed heating process was performed to obtain the dried aerogels: 130 °C (1 h), 140 °C (1 h), 150 °C (1 h), 200 °C (1 h), 300 °C (1 h) and 450 °C (1 h). The dried aerogels are nitrogen self-doped carbon/$BiVO_4$ aerogels, which are marked as NC/$BiVO_4$-10, where NC refers to the nitrogen self-doped carbon aerogels and 10 indicates that the initial TBOZ:$BiVO_4$ ratio is 10 wt%. The yields of the prepared NC/$BiVO_4$-10 and NC/$BiVO_4$-40 aerogels were 89.2% and 89.7%, respectively.

2.2.5 Synthesis of NC/$BiVO_4$-coated $Ni_{0.95}Zn_{0.05}(OH)_{2.0}$ aerogels

To obtain NC/$BiVO_4$-coated $Ni_{0.95}Zn_{0.05}(OH)_{2.0}$ aerogels, 5.0 g of the as-synthesized $Ni_{0.95}$Zn0.05(OH)2.0 were added simultaneously with TBOZ ahead of the preparation of NC/$BiVO_4$ aerogels. The remaining synthesis steps remained the same as 2.2.4. The obtained product was marked as NC/$BiVO_{4\text{-}x}$@$Ni_{0.95}Zn_{0.05}(OH)_{2.0}$. The synthesis details for NC/$BiVO_{4\text{-}x}$@$Ni_{0.95}$Zn0.05$(OH)_{2.0}$ were summarized in Table 1.

Table 1: Gelation and aging time for the tri-functional benzoxazine monomer derived NC/$BiVO_4$ monolithic aerogels.

Sample code	Monomer weight percent (%)	Gelation time (min)	Aging time (min)
NC/$BiVO_4$-10@$Ni_{0.95}Zn_{0.05}(OH)_{2.0}$	5	220	250
NC/$BiVO_4$-40@$Ni_{0.95}Zn_{0.05}(OH)_{2.0}$	20	120	120

2.2.6 Assembly of aqueous Ni-Zn batteries

Prior to cell assembly, the electrode materials were pretreated. The as-prepared NC/$BiVO_4$-x@$Ni_{0.95}Zn_{0.0}5(OH)_{2.0}$ aerogel served as the cathode, which was rinsed with deionized water and dried under nitrogen to remove surface impurities, ensuring a clean electrode surface. Zinc plates were used as the anode: after mechanical polishing to remove the oxide layer, they were activated by immersion in 0.1 M dilute sulfuric acid for 30 seconds, followed by rinsing with deionized water and drying. The pretreated NC/$BiVO_4$-x@$Ni_{0.95}Zn_{0.0}5(OH)_{2.0}$ aerogel cathode and zinc anode were placed face-to-face with an effective area of 1 cm², separated by a glass fiber membrane to maintain an electrode spacing of approximately 1 mm. The electrolyte was a ZnO-saturated 3 M potassium hydroxide (KOH) solution, prepared by adding excess ZnO powder (1-2 g/100 mL) to 3 M KOH, stirring for 24 hours, and filtering to ensure saturated Zn^{2+} concentration. Assembly was conducted in an argon-filled glovebox (H_2O < 0.1 ppm, O_2 < 0.1 ppm) to prevent contamination from atmospheric CO_2 and moisture. After sealing, the battery was left to stand for 12 hours to allow the electrolyte to fully infiltrate the electrode materials before electrochemical testing.

Based on the aqueous Ni-Zn batteries prepared by the above method, which can serve as energy storage units, they were further combined with a PERC solar module and a water electrolysis cell to construct a complete integrated solar-driven water-splitting system. The specific connection method and operation control of the system are as follows:

The integrated solar-driven water-splitting system was constructed by connecting a PERC solar module to two Ni-Zn batteries connected in series, and the water electrolysis cell. A double-pole double-throw (DPDT) switch was used to control the operational mode: in the 'DAY' position, the solar module powered the electrolyzer and charged the batteries simultaneously; in the 'NIGHT' position, the batteries discharged to power the electrolyzer independently.

2.3 Characterizations

The morphology and microstructural characteristics of the synthesized aerogels were studied by SEM (Nova NanoSEM50) and TEM (Talos F200X S/TEM) measurements. The diffraction properties and further crystal structure were studied by a X-ray diffractometer (Bruker D8 ADVANCE) equipped with a Cu Ka radiation (λ = 0.154178 nm). X-ray photoelectron spectroscopic (XPS) measurements were conducted on a X-ray photoelectron spectrometer equipped with a monochromatised Mg Kα X-ray source (AXIS Ultra, hv = 1283.3 eV). Raman spectra were collected on a Raman spectrometer (Jobin-Yvon HR 2000) to investigate the scattering features of the aerogels. The porous characteristics of the synthesized aerogels were investigated based on N_2 adsorption/desorption experiments (77 K) using a Micromeritics ASAP 2050 instrument. The specific surface areas, the pore size distribution and pore volumes of the synthesized aerogels were examined by the Brunauer-Emmett-Teller (BET) method. UV-Vis absorption spectra were collected using a UV-2600i spectrophotometer. Photoluminescence (PL) spectra were collected at room temperature using a nanometerics (RPM Blue) luminescence spectrometer.

2.4 Photoelectrochemical measurements

A BAS Epsilon Electrochemical workstation was used for the photoelectrochemical measurements. A three-compartment electrochemical cell was included in the workstation, namely the platinum foil, the Ag/AgCl electrode and the aerogels-coated foil, respectively. The NC/$BiVO_4$ aerogel-containing electrodes were prepared according to the following steps. Into a 50 mL beaker were added poly-vinylidenefluoride (PVDF, 0.05 g), dimethyl formamide (DMF, 5 mL), acetylene black (0.02 g) and the NC/$BiVO_4$ aerogel (0.1 g) under vigorous stirring for 10 h to form a fine suspension. Then the suspension was transferred into a foil via spin-coating. The formed film electrode was dried at 80 °C for 24 h to get rid of the DMF solvent. The photocurrent (i)-time (t) curves were collected under open circuit potential in ultrapure water. A 300 W Xe lamp was used as the light source. The electrochemical impedance spectroscopy (EIS) measurement was also performed under open circuit potential in ultrapure water. The test frequency ranged from 1 MHz to 0.01 Hz. The AC voltage amplitude was 5 mV. The linear sweep voltammograms (LSV) measurement was investigated using the H_2O_2 solution (10 mM) as the electrolyte. The scanning potential ranged from 0.5 V to -0.9 V vs. SCE. The scanning rate was 5 mV/s.

2.5 NMR spectroscopy experiments

Solution state ^1H and ^{13}C NMR spectra were conducted on a Bruker Avance 400 MHz spectrometer at room temperature with $CDCl_3$ as the deuterium reagent. Chemical shifts (δ, ppm) of the tested chemicals were recorded using tetramethylsilane as the internal standard.

The solid-state ^{19}F NMR spectra were collected on a Bruker Avance Neo spectrometer. Sample preparation was performed in an argon-filled glovebox: approximately 20 mg of dried aerogel powder was accurately weighed, and a 1 M NEt_4BF_4/acetonitrile solution (with a volume 120% of the total pore volume estimated from nitrogen adsorption data) was added using an equal-volume impregnation method. The sample was sealed and equilibrated for 24 hours to ensure uniform distribution of the electrolyte within the pore channels. The impregnated powder was then packed into a 2.5 mm ZrO_2 rotor and sealed. Hexafluorobenzene (C_6F_6, δ = -164.9 ppm) was used as a secondary reference, and the spectra were acquired using a high-power ^1H decoupled single-pulse sequence to record the characteristic chemical shifts of the electrolyte within the pore channels.

2.6 X-ray pair distribution function

The ex-situ X-ray total scattering data was measured on a Riguku D/MAX2550 diffractometer equipped with a Mo K-α source (λ = 0.7107 Å). The XRD measurements were carried out in transmission geometry at 25 °C. The samples used were placed in Kapton capillaries in advance. An empty Kapton capillary was also tested as the background. PDFGetX2 was used to collect the data for PDF patterns, namely G(r). Renorma lised PDFs, namely g(r), are calculated according to the Eq. (1):[27]

$$G(r)=4\pi r\rho_0(g(r)-1) \tag{1}$$

in which ρ_0 indicates the number density of the structure model for the calculation function.

2.7 Photocatalytic hydrogen peroxide (H_2O_2) evolution

The photocatalytic H_2O_2 generation was conducted in a custom-built reactor: 50 mg of catalyst, 40 mL of ultrapure water, and 10 mL of isopropanol (hole sacrificial agent) were mixed, with high-purity O_2 continuously purged (20 mL min^{-1}), followed by stirring and irradiation under visible light (300 W xenon lamp with a 420 nm cutoff filter). The reaction temperature was maintained at 25 ± 1 °C. The H_2O_2 concentration was determined by the titanium oxysulfate colorimetric method: 1 mL of the reaction solution was taken at regular intervals, centrifuged to remove the catalyst, and 0.5 mL of the supernatant was added to 1.0 mL of $TiOSO_4$ reagent (0.5 g dissolved in 50 mL of 1 M H_2SO_4). After standing for 10 minutes for color development, the absorbance was measured at 405 nm and quantified according to a standard curve (linear range 0-100 μM). This method avoids the interference of isopropanol in potassium permanganate titration. The number of electron transfers (n) was measured by a rotating ring-disk electrode (RRDE, Pt ring-GC disk, collection efficiency N=0.28) in O_2-saturated 0.1 M phosphate buffer (pH 7.0). In this case, the H_2O_2 molecules generated on the disk will be oxidized to O_2, leading to the change of the generated photocurrent, including the disk current (I_{disk}) and the ring current (I_{ring}). According to the detected I_{disk} and I_{ring}, as well as the collection efficiency of the RRDE experiment (N=0.28), the electron transfer number (n) can be calculated using the Eq. (2):[28]

$$n = \frac{4I_{disk}}{I_{disk} + I_{disk}/N} \tag{2}$$

2.8 Photocatalytic HER and OER

The photocatalytic overall water splitting without sacrificial agents was evaluated in a closed gas circulation system: 50 mg of catalyst and 50 mL of ultrapure water were added to the photoreactor. After degassing by argon bubbling for 30 minutes, the system was irradiated under visible light (300 W xenon lamp with a 420 nm cutoff filter), maintaining the temperature at 25 °C. The generated gases (H_2 and O_2) were quantitatively analyzed at regular intervals (e.g., hourly) by an online gas chromatograph (GC-TCD, 5Å molecular sieve column, Ar carrier gas at 50 mL min^{-1}), and the H_2/O_2 molar ratio was monitored (expected to be ≈2:1). The oxygen origin from water splitting was confirmed by $H_2{}^{18}O$ isotope labeling experiments (97 atom% ^{18}O) combined with GC-MS detection of $^{18}O_2$ (m/z = 36). Dark reactions were used as controls to exclude non-photo-driven processes. The apparent quantum efficiency (AQE) at a specific wavelength (*e.g.*, 420±10 nm) was calculated based on the hydrogen evolution rate:[29]

AQE= [(2*Number of evolved hydrogen molecules)/ Number of incident photons]*100% (3)

where the coefficient 2 corresponds to the stoichiometry of the overall water splitting reaction: $2H_2O \rightarrow 2H_2 + O_2$.

3. Results and discussion

The fabrication strategy for the phenolic resin-derived monolithic NC/$BiVO_4$@$Ni_{0.95}Zn_{0.05}(OH)_{2.0}$ aerogels is illustrated in Schemes 1, 2. Tri-functional benzoxazine monomer TBOZ was produced by the Mannich reaction (Schemes 1). Polybenzoxazine (PBOZ) was subsequently fabricated upon the thermal curing reaction, leading to the assembly of three-dimensional (3D) cross-linked networks. The formation of the tri-functional benzoxazine monomer TBOZ (Scheme 1a) and its ring-opening polymerization reaction (Scheme 1b) were the basis for the architecture of the phenolic resin derived monolithic aerogels (NC/$BiVO_4$). As illustrated in Scheme 2, $BiVO_4$ nanoparticles were synthesized via a hydrothermal process using OA and OLA as surfactants to facilitate Bi^{3+}/VO_4^{3-} ion transfer. The nanoparticles were then dispersed in acetone under sonication and freeze-dried, inducing restructuring into nanosheets through disassembly and reassembly. A range of PBOZ derived monolithic aerogels were constructed through acetic acid-catalyzed ring-opening polymerization of a branched benzoxazine monomer (TBOZ) and sol-gel processes at a large scale, in which layered $BiVO_4$ nanosheets were embedded in the pores of nitrogen self-doped carbon aerogels (NC).

The chemical structure of TBOZ was confirmed by ^1H

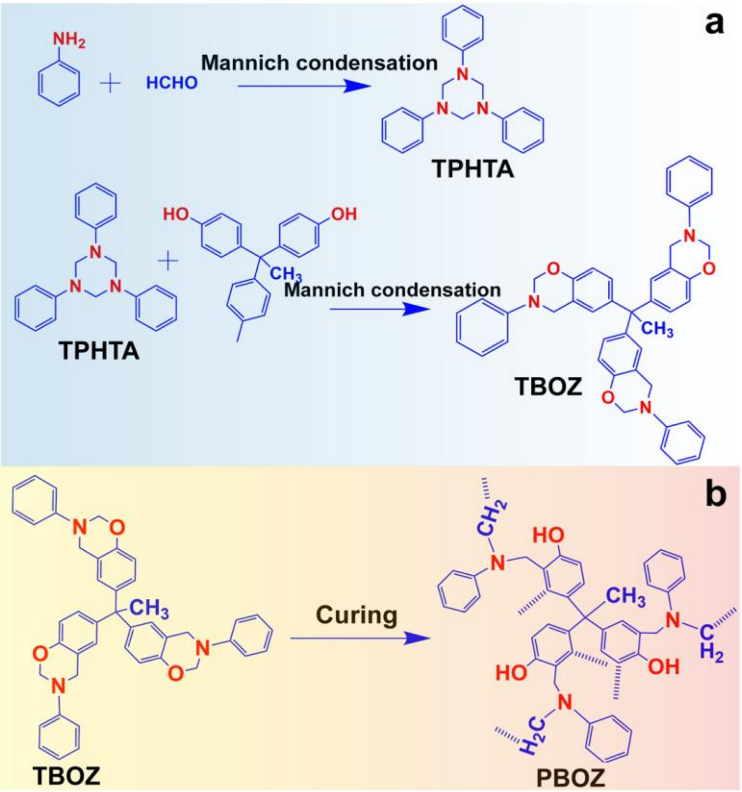

Scheme 1: (a) Synthetic pathway for the benzoxazine monomer and (b) its ring-opening polymerization reaction.

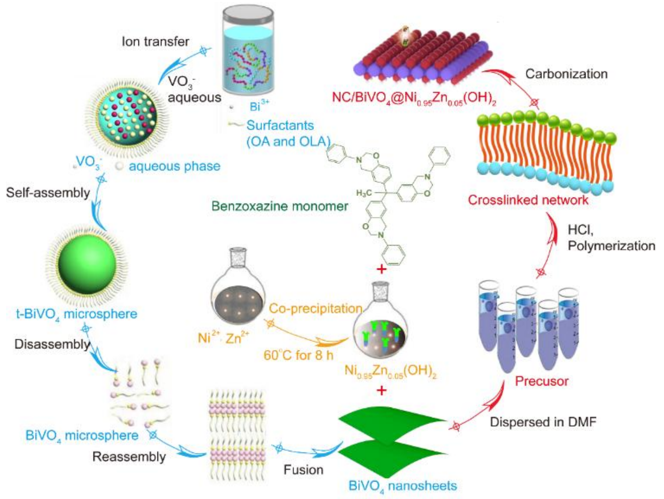

Scheme 2: The fabrication process of the phenolicres in derived monolithic aerogels.

NMR spectrum (Fig. 1a) and ^{13}C NMR spectrum (Fig. 1b). Then the monomer and the pre-prepared $BiVO_4$ nanosheets were proceeded acetic acid-catalyzed polymerization under the solution of acetic acid and DMF. After the gelation and aging processes under high temperature, abundant nitrogen self-doped carbon aerogels (NC) embedded into the layers of the $BiVO_4$ nanosheets, leading to the generation of hierarchical porous NC/$BiVO_4$ monolithic aerogels. The fabrication strategy was time-efficient and easily large-scale, allowing for a simple regulating of density and porosity by modifying the ratio of TBOZ monomer to acetic acid catalyst. The resultant $Ni_{0.95}Zn_{0.05}(OH)_{2.0}$-coated hierarchically porous NC/$BiVO_4$ aerogels (NC/$BiVO_4$@$Ni_{0.95}Zn_{0.05}(OH)_{2.0}$) had high specific surface area (758.54-929.21 m^2 g^{-1}), ultralow density (0.13-0.27 g cm^{-3}) and high electrical conductivity (31-58 S cm^{-1}) when the concentration of TBOZ ranging from 10 to 40%. The nanostructure of the NC/$BiVO_4$@$Ni_{0.95}Zn_{0.05}(OH)_{2.0}$ aerogel was studied by SEM (Fig. 1c) and TEM (Figs. 1d-g). The aerogel was highly fluffy, which was built by numerous ultrathin lamellae with the thickness of about ten to several ten μm. As a result of the stacking and crossing of these ultrathin lamellae, regularly distributed porous structure was formed. The elemental distribution mapping (Figs. 1h, i, j) demonstrated that the surface of NC/$BiVO_4$@$Ni_{0.95}Zn_{0.05}(OH)_{2.0}$ was indeed rich in C, despite that the C signal was weaker than that of Bi and V.

Fig. 2a presents the XRD patterns of the phase purity information of the aerogels, as well as the pristine few-layer $BiVO_4$ nanosheets and $Ni_{0.95}Zn_{0.05}(OH)_{2.0}$. All the diffraction peaks of the pristine $Ni_{0.95}Zn_{0.05}(OH)_2$ go perfectly with the standard XRD pattern of hexagonal β-$Ni(OH)_2$ (Fig. S1). It is clear that the width of the peaks for few-layer $BiVO_4$ increase

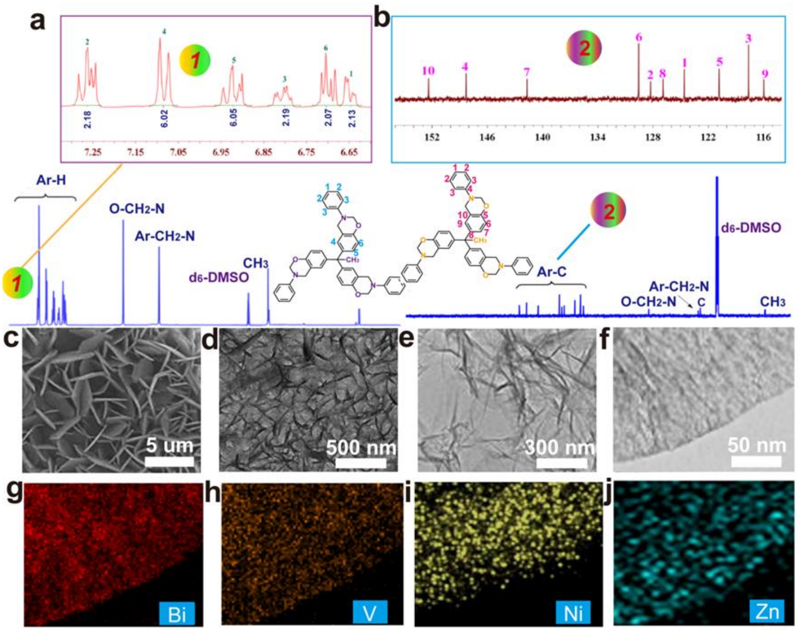

Fig. 1: Molecular and microstructural analysis of TBOZ and the aerogels. (a) ^1H NMR and (b) ^{13}C NMR spectra of TBOZ; (c) SEM image, (d) typical TEM image, (e, f) HRTEM images, and SEM-EDS elemental mapping images showing the distribution of Bi (g), V (h), Ni (i) and Zn (j) elements in the NC/$BiVO_4$-40@$Ni_{0.95}Zn_{0.05}(OH)_{2.0}$ aerogel.

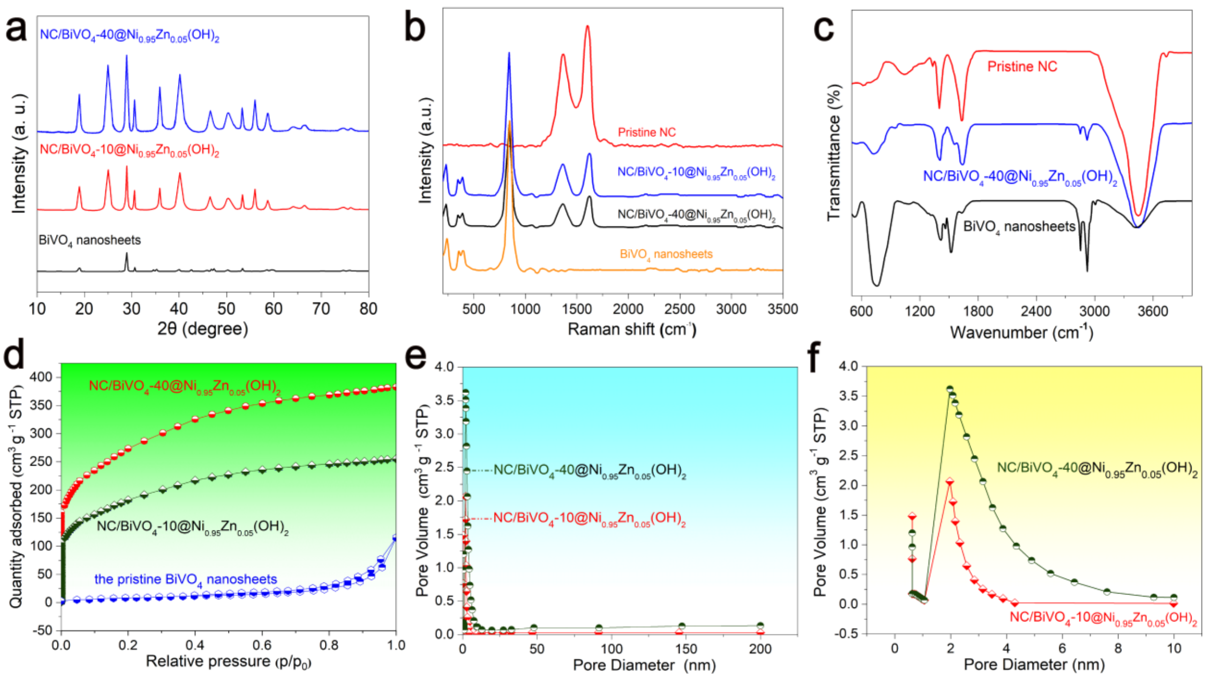

Fig. 2: Phase composition, molecular vibrations and pore structure. (a) XRD patterns of the NC/BiVO$_4$-10@Ni$_{0.95}$Zn$_{0.05}$(OH)$_{2.0}$, NC/BiVO$_4$-40@Ni$_{0.95}$Zn$_{0.05}$(OH)$_{2.0}$ aerogels and the pristine BiVO$_4$ nanosheets; (b) Raman spectra of the NC/BiVO$_4$-10@Ni$_{0.95}$Zn$_{0.05}$(OH)$_{2.0}$, NC/BiVO$_4$-40@Ni$_{0.95}$Zn$_{0.05}$(OH)$_{2.0}$ aerogels, the pristine BiVO$_4$ nanosheets and NC; (c) FT-IR spectra of the NC/BiVO$_4$-40@Ni$_{0.95}$Zn$_{0.05}$(OH)$_{2.0}$ aerogel, the pristine BiVO$_4$ nanosheets and NC; (d) Nitrogen adsorption–desorption isotherms of the NC/BiVO$_4$-10@Ni$_{0.95}$Zn$_{0.05}$(OH)$_{2.0}$, NC/BiVO$_4$-40@Ni$_{0.95}$Zn$_{0.05}$(OH)$_{2.0}$ aerogels and the pristine BiVO$_4$ nanosheets; (e) Pore size distribution of the NC/BiVO$_4$-10@Ni$_{0.95}$Zn$_{0.05}$(OH)$_{2.0}$ and NC/BiVO$_4$-40@Ni$_{0.95}$Zn$_{0.05}$(OH)$_{2.0}$ aerogels; (f) A magnification of the pore size distribution for the NC/BiVO$_4$-10@Ni$_{0.95}$Zn$_{0.05}$(OH)$_{2.0}$ and NC/BiVO$_4$-40@Ni$_{0.95}$Zn$_{0.05}$(OH)$_{2.0}$ aerogels ranging from 0-10 nm.

slightly, indicating that its crystal size becomes smaller and the crystallinity is lower than those of the bulk BiVO$_4$ (Fig. S2) due to the decrease of the number of layers. The characteristic peaks of the nitrogen self-doped carbon aerogels (NC) (27°), NC/BiVO$_4$-10 and NC/BiVO$_4$-40 are shown in Fig. S3 and Fig. S4. The diffraction peaks of the pristine BiVO$_4$ nanosheets are similar to aerogels, indicating that the incorporation of the nitrogen self-doped carbon aerogels (NC) does not damage the crystal phase of the BiVO$_4$ nanosheets. The difference of the diffraction peaks for both aerogels is that the characteristic peak at 27° can hardly be detected for NC/BiVO$_4$-10@Ni$_{0.95}$Zn$_{0.05}$(OH)$_{2.0}$ as a result of the relatively low amount of NC.

The Raman spectra of the monolithic aerogels, the pristine NC and BiVO$_4$ nanosheets are shown in Fig. 2b. There are two distinct characteristic peaks for the pristine NC, namely the D-band (1352 cm^{-1}) and the G-band (1586 cm^{-1}).[30] The relative high intensity of the G-band for the NC/BiVO$_4$-40@Ni$_{0.95}$Zn$_{0.05}$(OH)$_{2.0}$ aerogel indicated that the graphitization concentration of the NC content in the NC/BiVO$_4$-40@Ni$_{0.95}$Zn$_{0.05}$(OH)$_{2.0}$ aerogel was higher than that in the NC/BiVO$_4$-10@Ni$_{0.95}$Zn$_{0.05}$(OH)$_{2.0}$ aerogel, owing to the higher gelation and aging temperature in the polymerization of TBOZ. The characteristic peaks at 211, 322, 365, 712, and 826 cm^{-1} indicate that the pristine BiVO$_4$ nanosheets belong to a monoclinic phase.[31] The characteristic peaks of NC and BiVO4 still existed in the aerogels, demonstrating that NC/BiVO$_4$ aerogels were successfully prepared.

The chemical structure of the as-synthezised aerogel, the pristine NC and BiVO$_4$ nanosheets were examined by FT-IR spectra (Fig. 2c). There were four clear characteristic peaks for the pristine NC, namely the stretching vibration peaks of –OH (3440), C=C/C=O (1630), C-O-C (1052) and –COO (1393), respectively.[32] With regards to the pristine BiVO$_4$ nanosheets, the characteristic peak at 755 cm-1 was indexed to the stretching vibration of V-O. The broad band at 3441 cm^{-1} was corresponding to the stretching vibration of the H_2O molecules adsorbed on the surface of the BiVO$_4$ nanosheets. The dominated characteristic peaks of NC and BiVO$_4$ nanosheets were observed and no impure peaks existed in the NC/BiVO$_4$-40@Ni$_{0.95}$Zn$_{0.05}$(OH)$_{2.0}$ aerogel, indicating that NC has been successfully bonded to the BiVO$_4$ nanosheets.

The pore structure characteristics of the monolithic aerogels and the pristine BiVO$_4$ nanosheets were investigated by N_2 nitrogen adsorption-desorption isotherms (Fig. 2d). Typical IV isotherms were observed for both aerogels, suggesting that not only micropores ($<$2 nm), but also mesopores (2-50 nm) existed in the aerogels. The major N_2 adsorption behavior over the NC/BiVO$_4$ aerogels occurred at a relatively low pressure ($<$0.1), which demonstrated that both aerogels had high microporosity. The BET specific surface

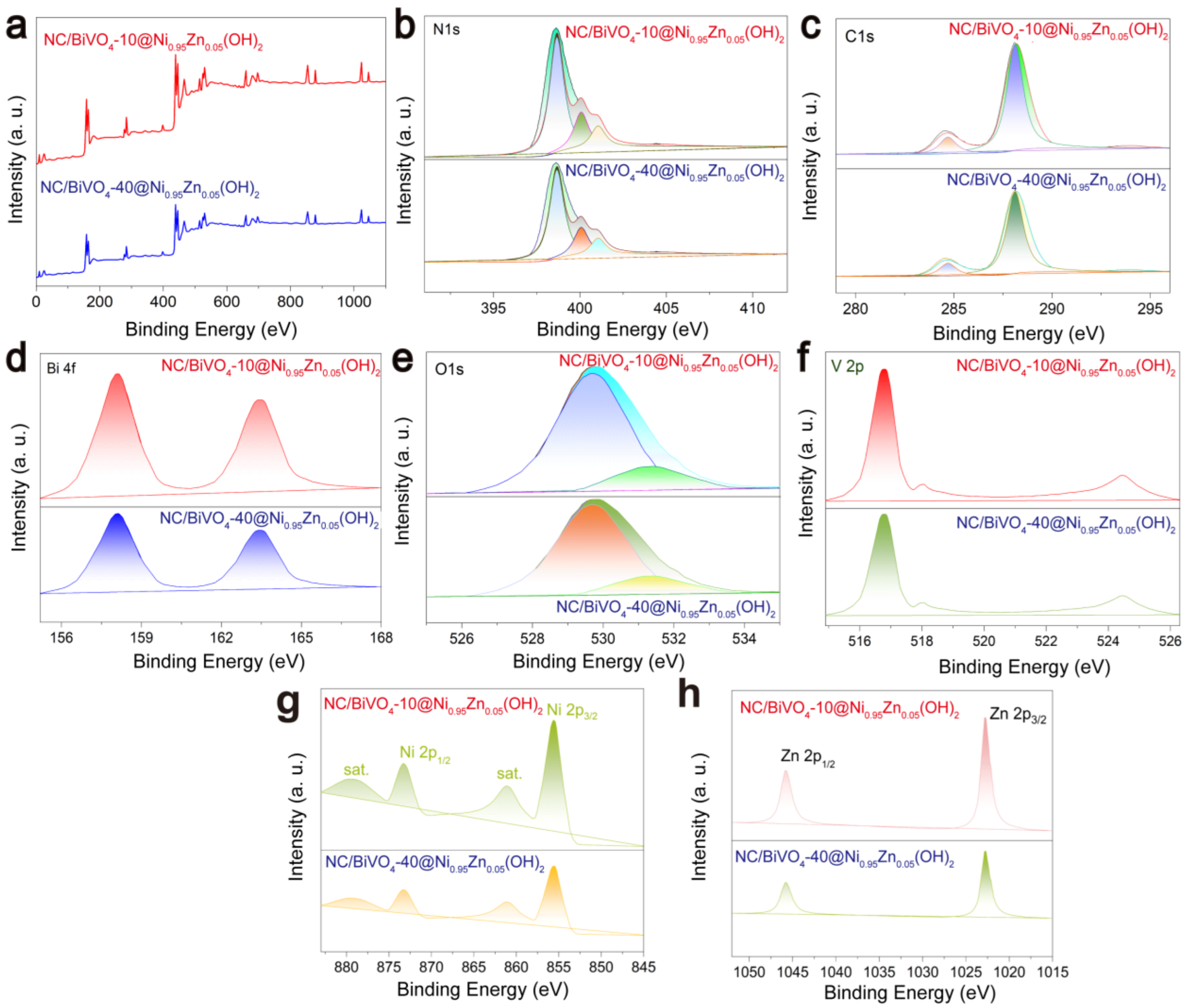

Fig. 3: XPS survey spectra and high-resolution elemental analysis. (a) XPS survey spectra of the NC/BiVO$_4$-10@Ni$_{0.95}$Zn$_{0.05}$(OH)$_{2.0}$ and NC/BiVO$_4$-40@Ni$_{0.95}$Zn$_{0.05}$(OH)$_{2.0}$ aerogels; (b) high-resolution N 1s, (c) C 1s, (d) Bi4f, (e) O 1s, (f) V2p, (g) Ni 2p and (h) Zn 2p spectra of the NC/BiVO$_4$-40@Ni$_{0.95}$Zn$_{0.05}$(OH)$_{2.0}$ aerogel.

areas (S_{BET}) of the pristine BiVO$_4$ nanosheets and the monolithic aerogels were calculated to be 28.38, 758.54 and 929.21 m^2 g^{-1}. The much higher BET data and the detailed pore size distribution information (Figs. 2e, f) indicated that both aerogels remained opened channels. On one hand, it endowed the aerogels with abundant active adsorption sites; On the other hand, these opened pores were beneficial to the transport and storage of the adsorbents and the adsorbents, as well as the release of the generated gas in the photocatalytic reactions.

The element composition of the aerogels and the chemical states of each element were examined by XPS. The survey XPS spectra (Fig. 3a) of the aerogels indicate that there are N, C, Bi, O V, Zn and Ni in the aerogels, as compared with that of NC/BiVO$_4$-10 and NC/BiVO$_4$-40 (Fig. S5). The percentages of the N, C, Bi, V, O, Zn and Ni components on the surface of both aerogels were listed in Table 2. The high resolution N 1s spectrum of NC/BiVO$_4$-40@Ni$_{0.95}$Zn$_{0.05}$(OH)$_{2.0}$ aerogel (Fig. 3b) can be fitted to three peaks situated at 401.02 eV, 400.05 eV and 398.56 eV, which are corresponding to the quaternary N, tertiary N and sp^2-hybridized nitrogen, respectively.[29] Likewise, three peaks located at about 284.6, 286.3 and 288.1 eV are present in the C 1s fine spectrum of C 1s (Fig. 3c), corresponding to the three different bonding mode of C-C, C-O and C=O, respectively.[29] Two clear peaks (158.4 and 163.3 eV) are observed in the high resolution spectrum of Bi 4f (Fig. 3d), which are indexed to Bi 4f7/2 and Bi 4f5/2, respectively.[33] Both the Bi 4f7/2 and the Bi 4f5/2 species have a valency of +3. The high resolution O 1s spectrum of NC/BiVO$_4$-40@Ni$_{0.95}$Zn$_{0.05}$(OH)$_{2.0}$ aerogel (Fig. 3e) can be deconvolved into two peaks situated at 529.5 and 531.7 eV, corresponding to the lattice oxygen of layered $Bi_2O_2^{2+}$ species and the H_2O molecules adsorbed on the surface of the aerogel, respectively. The high resolution V 2p spectrum of NC/BiVO$_4$-40@Ni$_{0.95}$Zn$_{0.05}$(OH)$_{2.0}$ aerogel (Fig. 3f) involves a sharp peak at 516.5 eV and a broad peak at 524.1 eV, which are indexed to V 2p3/2 and V 2p1/2, respectively.[34] Both the V 2p3/2 and V 2p1/2 species have a valency of +5. The high resolution Ni2p and Zn 2p spectra were shown in Fig. 3g and Fig. 3h, respectively. These data directly demonstrated that nitrogen self-doped carbon aerogels had been successfully introduced into the BiVO$_4$ nanosheets.

The light-trapping performance of the monolithic aerogels,

Table 2: The percentage of each element in the NC/$BiVO_4$-10@$Ni_{0.95}Zn_{0.05}(OH)_{2.0}$ and NC/$BiVO_4$-40@$Ni_{0.95}Zn_{0.05}(OH)_{2.0}$ aerogels.

Samples	Element percentage (%)						
	N	C	Bi	V	O	Ni	Zn
NC/$BiVO_4$-10@$Ni_{0.95}Zn_{0.05}(OH)_{2.0}$	1.33	6.85	35.54	8.67	10.88	34.69	2.04
NC/$BiVO_4$-40@$Ni_{0.95}Zn_{0.05}(OH)_{2.0}$	4.75	21.66	28.48	6.95	8.72	27.81	1.63

and the pristine $BiVO_4$ nanosheets were evaluated by UV-vis absorption spectra (Fig. 4a). Apparently, the incorporation of the nitrogen self-doped carbon aerogels in the layered structure of $BiVO_4$ nanosheets significantly promoted the light adsorption properties of the photocatalysts over the entire light radiation wavelength. Moreover, the absorption peak generated a red shift after the ratio of TBOZ monomer was increased in the NC/$BiVO_4$ aerogels. According to the Tauc's plot, optical band gap energy (E_g) of the pristine $BiVO_4$ nanosheets and the monolithic aerogels was calculated to be 2.40, 2.27 and 2.09 eV, respectively (Fig. 4b). It was obvious that the introduction of NC into $BiVO_4$ nanosheets could narrow the band gaps of the hybrids and stimulate the effective utilization of visible light with low energy and further the enhancement of the photocatalytic efficiency. The UPS spectra of the pristine $BiVO_4$ nanosheets and the monolithic aerogels were shown in Fig. 4c. Based on the linear intersection method, the maximum valence band (E_{VB}) of the pristine $BiVO_4$ nanosheets, the NC/$BiVO_4$-10@$Ni_{0.95}Zn_{0.05}(OH)_{2.0}$ and the NC/$BiVO_4$-40@$Ni_{0.95}Zn_{0.05}(OH)_{2.0}$ aerogels was determined to be 2.36, 2.16 and 1.69 eV, respectively. Therefore, the minimum conduction band (E_{CB}) of the pristine $BiVO_4$ nanosheets, NC/$BiVO_4$-10@$Ni_{0.95}Zn_{0.05}(OH)_{2.0}$ and the NC/$BiVO_4$-40@$Ni_{0.95}Zn_{0.05}(OH)_{2.0}$ aerogels was -0.40, -0.11 and -0.035 eV (*vs.* vacuum), respectively, according to the formula $E_g = E_{VB} - E_{CB}$. Consequently, the energy level diagram of the pristine $BiVO_4$ nanosheets, the aerogels was clearly present in Fig. 4d. On one hand, the conduction bands of NC/$BiVO_4$-10@$Ni_{0.95}Zn_{0.05}(OH)_{2.0}$ and the NC/$BiVO_4$-40@$Ni_{0.95}Zn_{0.05}(OH)_{2.0}$ aerogels are above the reduction level for H_2O to H_2; on the other hand, the valence band of NC/$BiVO_4$-10@$Ni_{0.95}Zn_{0.05}(OH)_{2.0}$ and the NC/$BiVO_4$-40@$Ni_{0.95}Zn_{0.05}(OH)_{2.0}$ aerogels are under the oxidation level for H_2O to H_2O_2 or O_2.

Therefore, these properly distributed bands of the as-synthesized NC/$BiVO_4$ aerogels are beneficial for the transfer of electrons and holes, respectively, in this way endowing the NC/$BiVO_4$ aerogels with the ability of both the water reduction and oxidation.

The as-synthesized NC/$BiVO_4$@$Ni_{0.95}Zn_{0.05}(OH)_{2.0}$

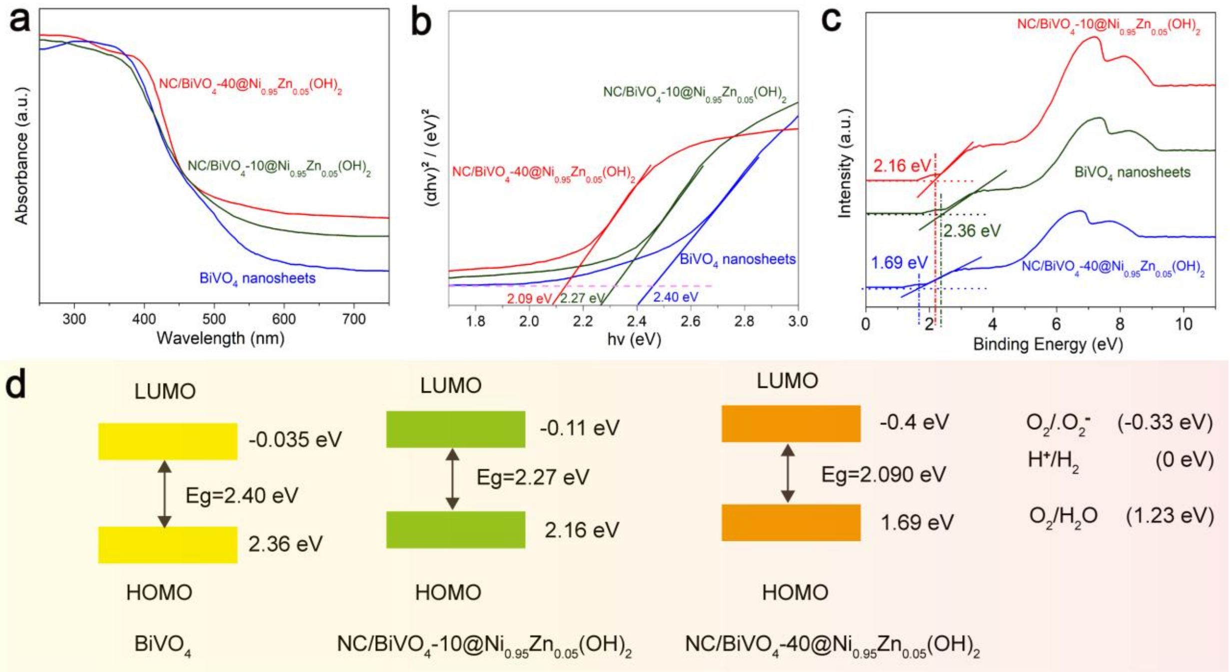

Fig. 4: Photoelectric properties and band structure characterization. (a) UV-vis absorption spectra of the NC/$BiVO_4$-10@$Ni_{0.95}Zn_{0.05}(OH)_{2.0}$, NC/$BiVO_4$-40@$Ni_{0.95}Zn_{0.05}(OH)_{2.0}$ aerogels and the pristine $BiVO_4$ nanosheets; (b) $(\alpha h\nu)^2$ versus hν curve of the NC/$BiVO_4$-10@$Ni_{0.95}Zn_{0.05}(OH)_{2.0}$, NC/$BiVO_4$-40@$Ni_{0.95}Zn_{0.05}(OH)_{2.0}$ aerogels and the pristine $BiVO_4$ nanosheets; (c) Ultraviolet photoelectron spectroscopy (UPS) of the NC/$BiVO_4$-10@$Ni_{0.95}Zn_{0.05}(OH)_{2.0}$, NC/$BiVO_4$-40@$Ni_{0.95}Zn_{0.05}(OH)_{2.0}$ aerogels and the pristine $BiVO_4$ nanosheets and (d) Band structure diagram for the NC/$BiVO_4$-10@$Ni_{0.95}Zn_{0.05}(OH)_{2.0}$, NC/$BiVO_4$-40@$Ni_{0.95}Zn_{0.05}(OH)_{2.0}$ aerogels, in comparison with the pristine $BiVO_4$ nanosheets.

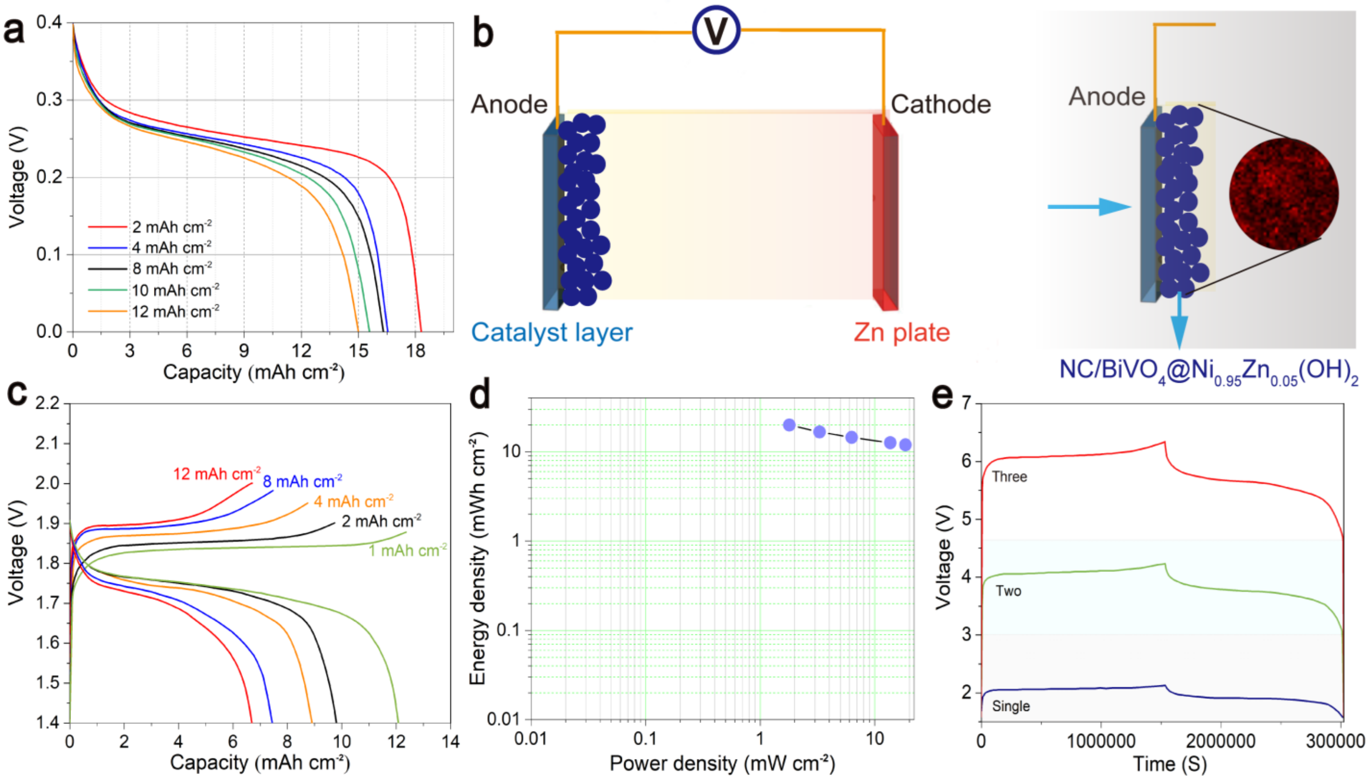

Fig. 5: Electrode behavior, device configuration and electrochemical performance. (a) Discharge behavior toward the as-synthesized NC/$BiVO_4$-40@$Ni_{0.95}Zn_{0.05}(OH)_{2.0}$ aerogel. (b) Diagram of the self-made aqueous Ni-Zn battery based on the NC/$BiVO_4$-40@$Ni_{0.95}Zn_{0.05}(OH)_{2.0}$ aerogel. (c) GCD curves of the Ni-Zn battery. (d) Areal energy and power densities of the Ni-Zn battery. (e) Charge-discharge curves of the Ni-Zn batteries connected in series.

aerogels can perform well in the electrochemical reaction under strong alkaline electrolyte (KOH, 1 M). As shown in Fig. 5a, the NC/$BiVO_4$-40@$Ni_{0.95}Zn_{0.05}(OH)_{2.0}$ electrode exhibits favorable discharge performance with current densities ranging from 2 to 12 mA cm^{-2}. Obviously, the capacity of the NC/$BiVO_4$-40@$Ni_{0.95}Zn_{0.05}(OH)_{2.0}$ electrode is as high as 18.4 mAh cm^{-2} at a current density of 2 mA cm^{-2} and maintains 14.9 mAh cm^{-2} as the current density raises to 12 mA cm^{-2}. The assembled Ni-Zn battery is illustrated in Fig. 5b, in which the NC/$BiVO_4$-10@$Ni_{0.95}Zn_{0.05}(OH)_{2.0}$ aerogel and the Zn plate is used as the cathode and the anode, respectively. High charge and discharge plateaus can be observed in the GCD curves under different current densities (Fig. 5c). It is worth mentioning that an impressive areal capacity of 12.4 mAh cm^{-2} can be acquired for the as-assembled Ni-Zn battery, substantially outperforming most previously reported aqueous batteries.[22] As shown in Fig. 5d, both the areal energy and the power densities of the as-assembled Ni-Zn battery are outstanding. The energy density for our device is as high as 12.1 mWh cm^{-2} at a current density of 2 mA cm^{-2}. Moreover, the single Ni-Zn battery can be integrated in series so as to obtain higher operating voltages for practical applications (Fig. 5e).

A set of integrated device is illustrated in Fig. 6a, in which the solar passivated emitter and rear cell (PERC) is used to charge the assemble Ni-Zn battery. The open-circuit voltage of the PSSC device is as high as 9.9 V. Besides, its short-circuit current is 12.2 mA under AM 1.5 illumination (Fig. S6). It can be clearly observed that PERC has excellent stability (Fig. 6b). Apparently, the charging plateaus of the Ni-Zn battery kept rising as the light intensity increased (Fig. 6c). After solar charged by PSSC, a voltage of 2.14 V could be aquired for the assembled Ni-Zn battery (Fig. 6d). In addition, it could be galvanostatically discharged to 1.57 V with a current density of 2 mA cm^{-2} in 3024000 s. Given the impressive bifunctional catalytic activities observed, the steady-state polarization curve for overall water splitting of NC/$BiVO_4$-40@$Ni_{0.95}Zn_{0.05}(OH)_{2.0}$ aerogel was measured (Fig. 6e), which exhibited a current density of 21.5 mA cm^{-2} with an external bias of 1.741 V. Such a solar-charged Ni-Zn battery is expected to drive overall water splitting without interruption. Besides, a potential of 1.772 V is required to attain a current density of 50 mA cm-2, which shows that a clear voltage difference (ΔV) between the HER (Fig. 6f) and OER (Fig. 6g). These comparisons suggest the practical application of our solar-charged Ni-Zn battery.

As illustrated in Fig. 7a-b, the self-driven solar-powered uninterrupted overall water-splitting device achieves 24-hour operation via a dual-mode system, which integrates a PERC module (or PSSC, as referenced) and fully solar-charged Ni-Zn batteries. Specifically, during the daytime (0-12 h), the PERC module-featuring a high open-circuit voltage of 9.9 V (Fig. S6)-fulfills two key functions: it not only provides sufficient potential to drive the electrolyzer but also charges

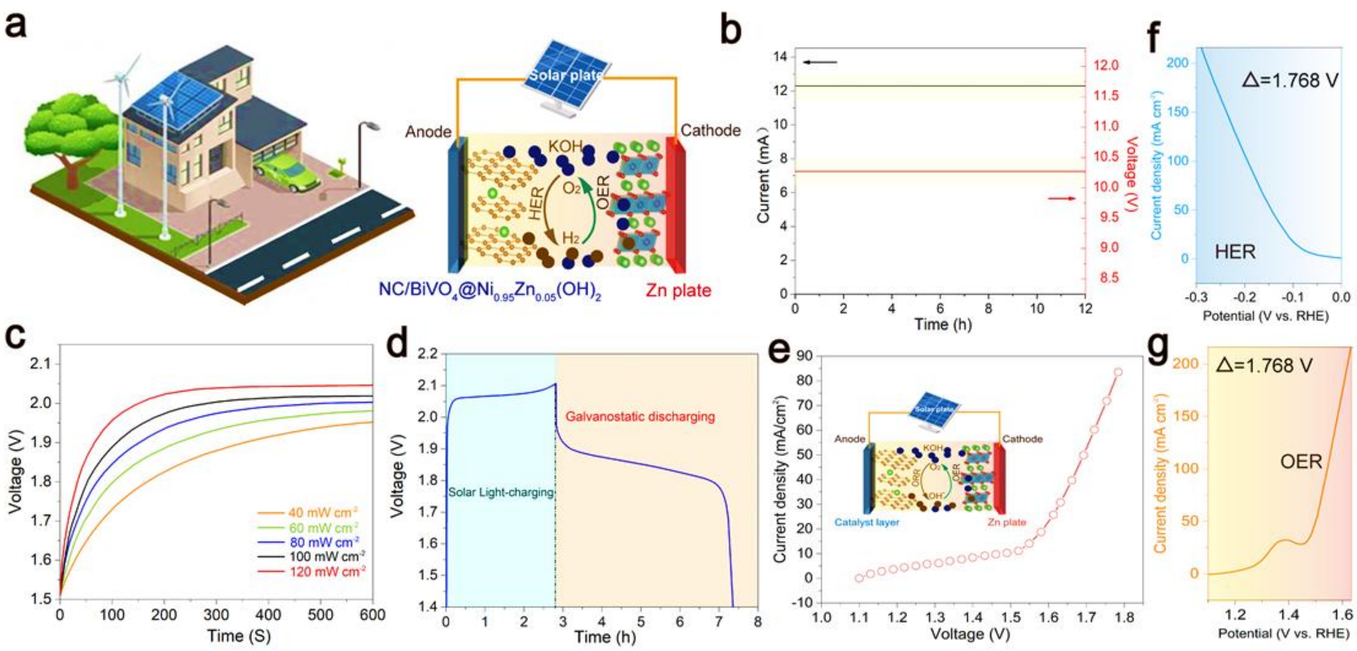

Fig. 6: Performance of Ni - Zn battery (PERC - charged) and aerogel catalysts under AM 1.5 Illumination and in 1 M KOH. (a) Schematic illustration of the assembled Ni-Zn battery charged by PERC. (b) Open-circuit voltage and short-circuit current of PERC irradiated by AM 1.5 illumination for 12 h. (c) Ni-Zn battery charged under different light intensities for the same duration of illumination. (d) Light-charge and galvanostatic discharge performance of the solar-charged Ni-Zn battery. (e) Polarization curves of NC/$BiVO_4$-10@$Ni_{0.95}Zn_{0.05}(OH)_{2.0}$ for overall water splitting in 1 M KOH solution at a scan rate of 5 mV s^{-1} (inset: diagram of overall water splitting). Polarization curves of NC/$BiVO_4$-10@$Ni_{0.95}Zn_{0.05}(OH)_{2.0}$ for HER (f) and OER (g).

two series-connected Ni-Zn batteries (with a nominal voltage of ~3.6 V). The series connection between the PERC module and the two Ni-Zn batteries during this period is clearly depicted in Fig. 7c; specific data further confirm that the PERC device maintains a stable bias of 2.13 V across the two-electrode overall water-splitting device for 12 hours, as shown in the voltage-time curves of Fig. 7e.

When entering the nighttime (12-24 h), the system seamlessly switches to the pre-charged battery pack (note: the PERC module cannot charge the batteries at night due to insufficient sunlight, which corrects the prior statement). At this stage, the battery pack delivers a stable discharge

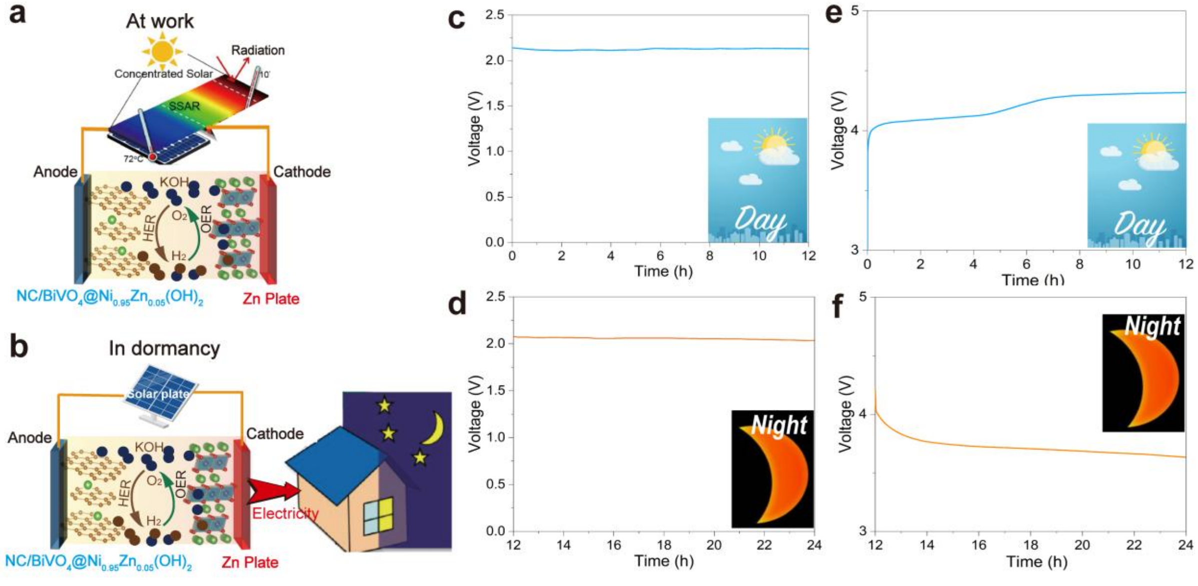

Fig. 7: Day-night solar hydrogen production system and energy storage integration. Fully solar-powered water-splitting system working non-stop during day (a) and night (b). (c) Voltage-time curve of self-driven overall water splitting powered by a PERC (0-12 h) and (d) two series-connected solar-charged Ni-Zn batteries (12-24 h). (e) Charging curve of two series-connected Ni-Zn batteries charged by a PSSC (0-12 h) and (f) the discharging curve of the Ni-Zn batteries during the self-driven overall water-splitting process (12-24 h).

voltage-specifically, a working voltage of 2.07 V for the water-splitting device (Fig. 7d)-which is adequate to sustain the water-splitting process. This is evidenced by the constant operating voltage observed in Fig. 7d. Additionally, the corresponding discharge curve in Fig. 7f further indicates that the Ni-Zn batteries can maintain a stable discharge plateau throughout the night, thereby demonstrating that the assembled rechargeable Ni-Zn batteries are capable of storing sufficient solar energy.

With regards to the photocatalytic activities of the as-synthesized aerogels, no any sacrificial agent or cocatalyst was used in the photocatalytic water dissociation. Under the irradiation of the Xe lamp (300 W) for 10 h, 30.5 and 57.8 μmol H_2 could be detected by gas chromatography (GC) over the aerogels, respectively (Fig. 8a). Nevertheless, only 4.8 μmol H_2 could be detected for the pristine $BiVO_4$ nanosheets. Obviously, NC/$BiVO_4$-40@$Ni_{0.95}Zn_{0.05}(OH)_{2.0}$ exhibited the fastest rate of H_2 production among all the samples. The overall photocatalytic water splitting performance of NC/$BiVO_4$-10@$Ni_{0.95}Zn_{0.05}(OH)_{2.0}$ and the NC/$BiVO_4$-40@$Ni_{0.95}Zn_{0.05}(OH)_{2.0}$ was compared in Fig. 8b and Fig. 8c, respectively. The evolution of O_2 was still quantified by GC (Fig. S7). The evolution rates of H_2 and O_2 over NC/$BiVO_4$-10@$Ni_{0.95}Zn_{0.05}(OH)_{2.0}$ and NC/$BiVO_4$-40@$Ni_{0.95}Zn_{0.05}(OH)_{2.0}$ were 3.05 (H_2), 1.50 (O_2), 5.78 (H_2), 2.85 (O_2) μmol h^{-1}, respectively. That is, the NC/$BiVO_4$-40@$Ni_{0.95}Zn_{0.05}(OH)_{2.0}$ aerogel still maintain the highest level of H_2 and O_2 production, and the evolution rates of H_2 and O_2 are almost stoichiometric ratio (2.03). During the whole water splitting reaction, no other gas (such as CO_2 or N_2) could be monitored by GC, suggesting that the aerogels had not been decomposed by the light irradiation and photocatalytic water splitting process. The water dissociation rate over the NC/$BiVO_4$-40@$Ni_{0.95}Zn_{0.05}(OH)_{2.0}$ aerogel still maintained high level even after 35 cycles (Fig. 8d), which demonstrated that the designed aerogels had good cycling stability. The slight decrease of H_2 and O_2 evolution rates may primarily due to the loss of the aerogel during the cyclic test. The good stability of the advanced NC/$BiVO_4$@$Ni_{0.95}Zn_{0.05}(OH)_{2.0}$ monolithic aerogels was ascribed to its structural stability (Fig. S8). AQE is an effective parameter to evaluate the electron/hole interaction in the photocatalytic H_2 evolution. The AQE of the aerogels and the pristine $BiVO_4$ nanosheets for H_2 evolution was depicted in Fig. 8e. It can be seen that the AQE value of all the samples decreased with the increase of the irradiation wavelength. The AQE value of NC/$BiVO_4$-40@$Ni_{0.95}Zn_{0.05}(OH)_{2.0}$ at 380 and 400 nm was 12.8% and 9.7%, respectively. After the irradiation wavelength was increased to λ = 450 nm, the AQE value reached 11.5%, which was about 13 times higher than the pristine $BiVO_4$ nanosheets (0.88%). When the irradiation wavelength was above 600 nm, the AQE rapidly declined to zero for all the samples.

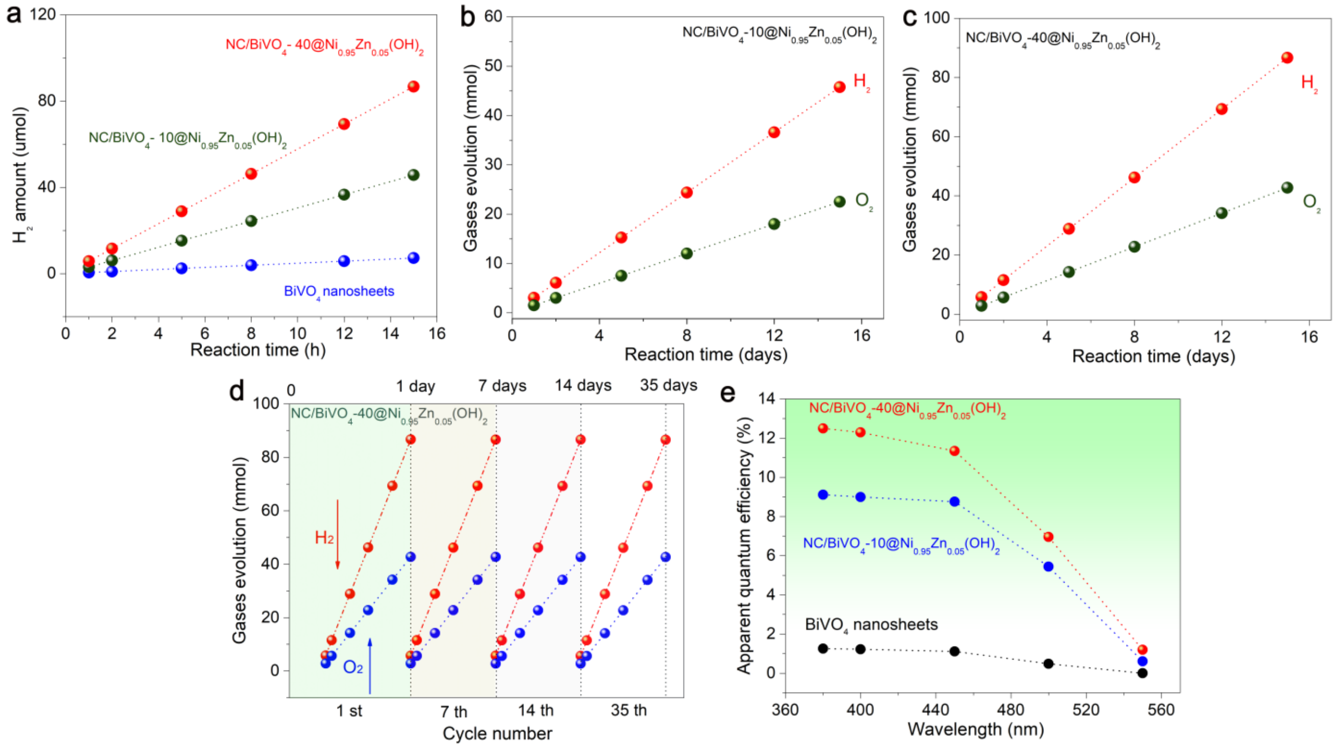

Fig. 8: Photocatalytic performance. (a) Photocatalytic H_2 evolution over the NC/$BiVO_4$-10@$Ni_{0.95}Zn_{0.05}(OH)_{2.0}$, NC/$BiVO_4$-40@$Ni_{0.95}Zn_{0.05}(OH)_{2.0}$ aerogels and the pristine $BiVO_4$ nanosheets under visible light irradiation (300 W Xe lamp (λ > 400 nm)); Time-gases output relationship over (b) NC/$BiVO_4$-10@$Ni_{0.95}Zn_{0.05}(OH)_{2.0}$ and (c) NC/$BiVO_4$-40@$Ni_{0.95}Zn_{0.05}(OH)_{2.0}$ aerogel; (d) Stability test of NC/$BiVO_4$-40@$Ni_{0.95}Zn_{0.05}(OH)_{2.0}$ aerogel. (e) AQE of NC/$BiVO_4$-10@$Ni_{0.95}Zn_{0.05}(OH)_{2.0}$ and NC/$BiVO_4$-40@$Ni_{0.95}Zn_{0.05}(OH)_{2.0}$ aerogels for H_2 evolution.

The H_2O_2 molecules are one of the important reactive species in the photocatalytic O_2 reduction reaction over the NC/$BiVO_4$ aerogels. The clear UV-vis absorption situated at 436 nm demonstrated that H_2O_2 was generated in the NC/$BiVO_4$ photocatalytic system (Fig. 9a). Figs. 9b, c further indicated that the NC/$BiVO_4$-10@$Ni_{0.95}Zn_{0.05}(OH)_{2.0}$ and NC/$BiVO_4$-40@$Ni_{0.95}Zn_{0.05}(OH)_{2.0}$ aerogels exhibited better photocatalytic activity than that of the pristine $BiVO_4$ nanosheets. The detailed H_2O_2 production amounts in 24 h over the $BiVO_4$ nanosheets, NC/$BiVO_4$-10@$Ni_{0.95}Zn_{0.05}(OH)_{2.0}$ and NC/$BiVO_4$-40@$Ni_{0.95}Zn_{0.05}(OH)_{2.0}$ were 48, 377 and 413 μmol g^{-1}, respectively (Fig. 9d). The LSV curves in Fig. 9e showed that the current density of NC/$BiVO_4$-40@$Ni_{0.95}Zn_{0.05}(OH)_{2.0}$ was highest than that of NC/$BiVO_4$-10@$Ni_{0.95}Zn_{0.05}(OH)_{2.0}$ and the $BiVO_4$ nanosheets, suggesting that NC/$BiVO_4$-40@$Ni_{0.95}Zn_{0.05}(OH)_{2.0}$ had an excellent catalytic ability in H_2O_2 degradation. The photocurrents increased linearly with the increase of light intensities, indicating no back reactions occurred in the photocatalytic O_2 reduction process (Fig. 9f). According to the current-light intensity curves, the value of I_{ring}/I_{disk} is nearly the same under different ω, contributing to the determination of n (n ≈ 2). Therefore, it can be confirmed that the CB electrons of NC/$BiVO_4$-40@$Ni_{0.95}Zn_{0.05}(OH)_{2.0}$ aerogel can reduce O_2 through two-electron process to form H_2O_2: $O_2 + 2H^+ + 2e^- \rightarrow H_2O_2$.

In order to clarify the synergistic effect between N-doped carbon and $BiVO_4$ and the wide variations in photocatalytic performance of the as-synthesized aerogels, solid-state ^{19}F NMR spectroscopy assay was conducted to study the influence of pore structural order on photocatalytic H_2 and O_2 evolution (Fig. 10a). There were two resonances in the ^{19}F NMR spectra of the electrolyte-saturated aerogels and the pristine NC. One resonance situated at about -150 ppm are corresponding to "ex-pore" anions, while the other resonances situated at lower chemical shifts are corresponding to "ex-pore" anions.[35] The detailed difference value between these two resonances (Δδ) involved was shown in Fig. 10b, which indicated that the introduction of $BiVO_4$ nanosheets into the pores of carbon aerogels increased the structural disorder of the hybrids. The structural disorder degree followed the orders: NC/$BiVO_4$-40@$Ni_{0.95}Zn_{0.05}(OH)_{2.0}$ ＞NC/$BiVO_4$-10@$Ni_{0.95}Zn_{0.05}(OH)_{2.0}$ ＞the pristine NC. The results of PDF patterns of the hybrids were also consistent with the ^{19}F NMR spectra (Fig. 10c). Comparing the X-ray PDF pattern of the aerogels and the pristine NC, we found that the local structural disorder governed the photocatalytic performance, with more disordered carbons with smaller ordered domains exhibiting higher yields of H_2 and O_2. The exsitu NMR measurements detected the concentration of in-pore cations and anions under different charging voltages (Fig. 10d). It was apparent that not only the cation uptake capacity but also the anion uptake capacity of the aerogels increased with the raise of the applied cell voltage. Importantly, the more disordered carbon in NC/$BiVO_4$-40@$Ni_{0.95}Zn_{0.05}(OH)_{2.0}$ showed agreater capacity to adsorb and store ions than the more ordered carbon (NC/$BiVO_4$-10@$Ni_{0.95}Zn_{0.05}(OH)_{2.0}$), suggesting that aerogels with smaller ordered domains gave rise to better photocatalytic performance.

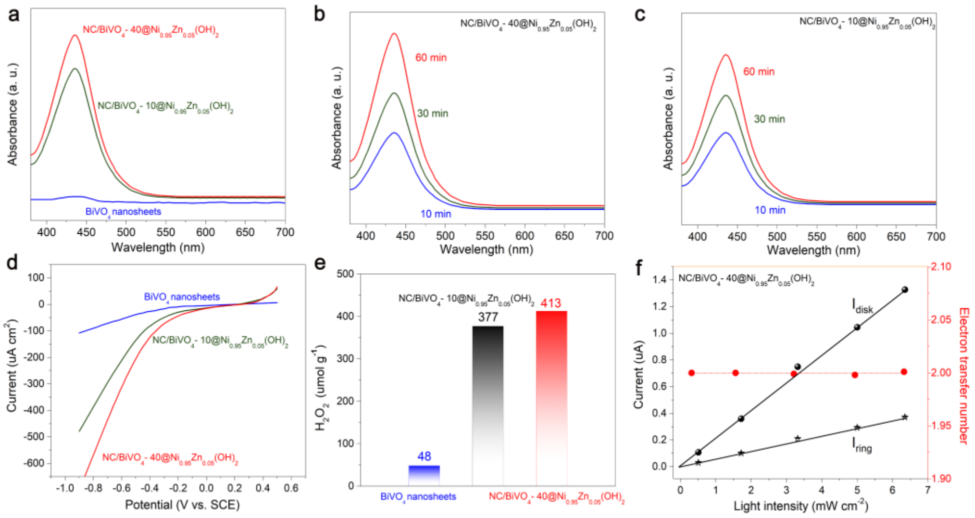

Fig. 9: Photocatalytic H_2O_2 production and electrocatalytic ORR performance. (a) The generation of H_2O_2 monitored by UV–vis absorption spectra in the catalytic system of the NC/$BiVO_4$-10@$Ni_{0.95}Zn_{0.05}(OH)_{2.0}$, NC/$BiVO_4$-40@$Ni_{0.95}Zn_{0.05}(OH)_{2.0}$ aerogels and the pristine $BiVO_4$ nanosheets; Time-resolved adsorption spectra of H_2O_2 solution in the catalytic system of (b) the NC/$BiVO_4$-40@$Ni_{0.95}Zn_{0.05}(OH)_{2.0}$ aerogel and (c) the NC/$BiVO_4$-10@$Ni_{0.95}Zn_{0.05}(OH)_{2.0}$ aerogel; (d) H_2O_2 production amount in the catalytic system of the NC/$BiVO_4$-10@$Ni_{0.95}Zn_{0.05}(OH)_{2.0}$, NC/$BiVO_4$-40@$Ni_{0.95}Zn_{0.05}(OH)_{2.0}$ aerogels and the pristine $BiVO_4$ nanosheets; (e) The LSV curves for the NC/$BiVO_4$-10@$Ni_{0.95}Zn_{0.05}(OH)_{2.0}$, NC/$BiVO_4$-40@$Ni_{0.95}Zn_{0.05}(OH)_{2.0}$ aerogels and the pristine $BiVO_4$ nanosheets; (f) RRDE collection measurements for oxygen reduction reaction catalyzed by the NC/$BiVO_4$-40@$Ni_{0.95}Zn_{0.05}(OH)_{2.0}$ aerogel. The NC/$BiVO_4$-40@$Ni_{0.95}Zn_{0.05}(OH)_{2.0}$ aerogel can achieve almost the same electron transfer number (n≈2)under different light intensity.

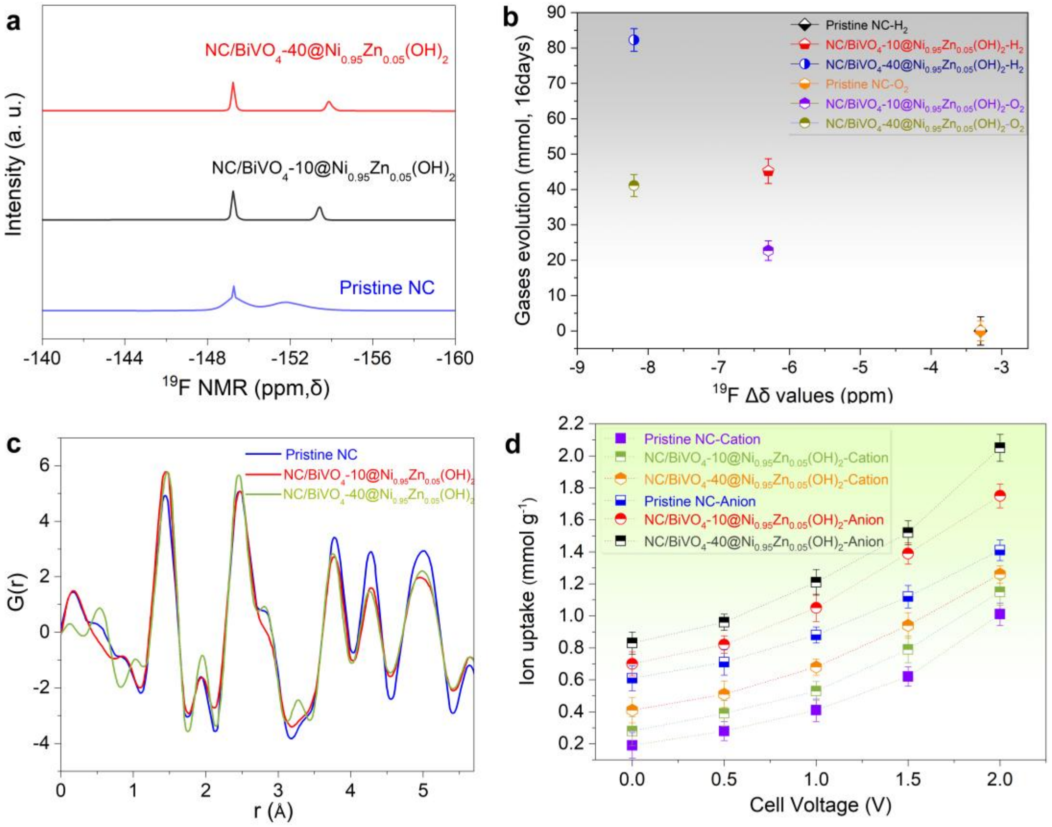

Fig. 10: Structural disorder and ion storage characterization of the aerogels for photocatalytic performance. (a) ^{19}F MAS NMR spectra of the as-synthesized photocatalysts soaked with 0.5 M NEt_4BF_4(ACN). (b) Correlation between ^{19}F Δδ values and photocatalytic H_2 and O_2 evolution. (c)The X-ray PDF patterns and (d) ion uptake capacity of the $NC/BiVO_4$-10@ $Ni_{0.95}Zn_{0.05}(OH)_{2.0}$, $NC/BiVO_4$-40@$Ni_{0.95}Zn_{0.05}(OH)_{2.0}$ aerogels and the pristine NC.

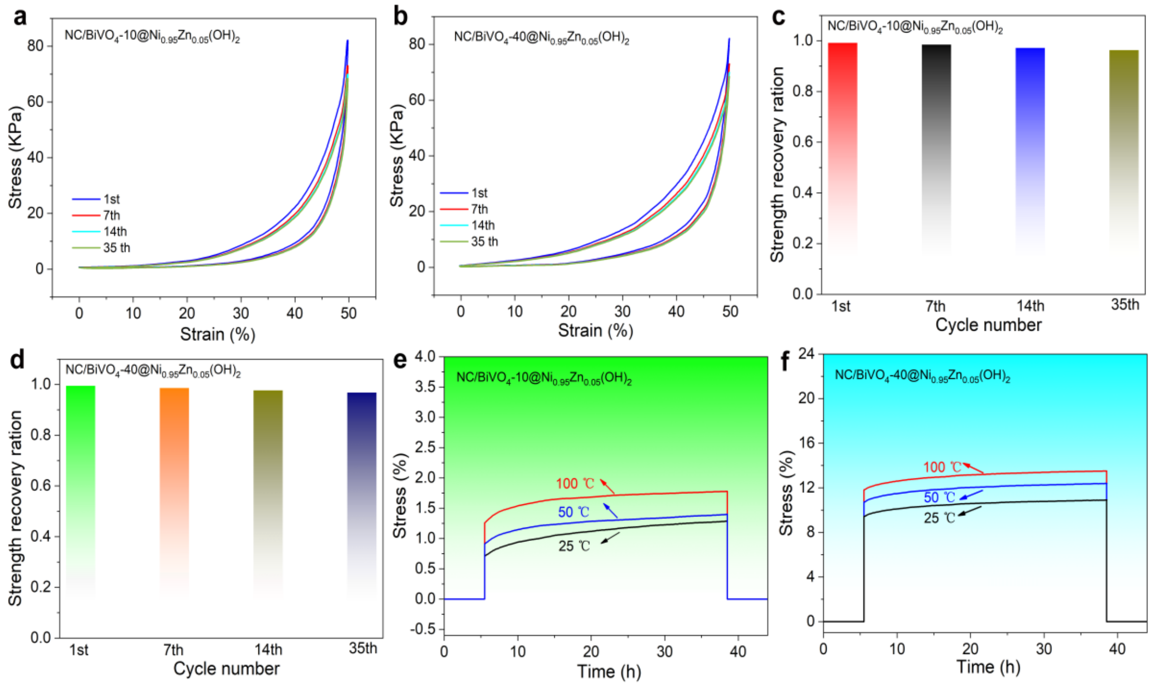

Fig. 11: Cyclic compression resilience, strength recovery and thermal creep behavior. The compression cycle of (a) $NC/BiVO_4$-10@ $Ni_{0.95}Zn_{0.05}(OH)_{2.0}$ and (b) $NC/BiVO_4$-40@ $Ni_{0.95}Zn_{0.05}(OH)_{2.0}$ after different photocatalytic water splitting cycles. Strength recovery ratio of (c) $NC/BiVO_4$-10@ $Ni_{0.95}Zn_{0.05}(OH)_{2.0}$ and (d) $NC/BiVO_4$-40@ $Ni_{0.95}Zn_{0.05}(OH)_{2.0}$ after different photocatalytic water splitting cycles. Creep curves of (e) $NC/BiVO_4$-10@ $Ni_{0.95}Zn_{0.05}(OH)_{2.0}$ and (f) $NC/BiVO_4$-40@ $Ni_{0.95}Zn_{0.05}(OH)_{2.0}$ after different photocatalytic water splitting cycles under a constant of 1 kPa for 1 h at three different temperatures (25, 50, and 100 °C).

The above characterization reveals a definitive structure-activity relationship. The polymerization behavior of the TBOZ monomer, regulated by its initial concentration, directly determines the microstructural disorder of the resultant NC matrix. A higher degree of disorder, as evidenced by ^{19}F NMR and PDF analysis, creates a more favorable environment for the adsorption and storage of reactive ions, such as OH^-. This enhanced ion storage capacity at the catalyst interface plays a pivotal role in promoting the separation of photogenerated charge carriers by facilitating the surface reaction kinetics, thereby leading to the dramatically improved photocatalytic performance observed in the NC/$BiVO_4$-40 aerogel.

The mechanical stability of bulk aerogel photocatalytic materials is of great significance in practical applications, as it ensures the structural integrity of materials in dynamic environments such as water flow scouring and vibration, avoids the decay of catalytic activity and engineering failures caused by fragmentation, and serves as a key prerequisite for realizing their large-scale applications in water treatment, air purification and other fields. Compressive stress-strain curves at 50% strain (Figs. 11a, b) for the monolithic aerogel photocatalysts NC/$BiVO_4$-10@ $Ni_{0.95}Zn_{0.05}(OH)_{2.0}$ and NC/$BiVO_4$-40@ $Ni_{0.95}Zn_{0.05}(OH)_{2.0}$ after different cycles revealed their resilience to repeated reactor handling and fluid flow. Initially, stress increased with strain, indicating elastic behavior; with progressing cycles, stable stress and high curve overlap demonstrated strong fatigue resistance and minimal irreversible damage, enabling the materials to maintain mechanical integrity under dynamic "compression-release" and fluid flow, thereby reducing fracture risk. The compressive stress-strain curves after 50 cycles (Figs. 11a, b) show high overlap with the initial cycles, and the calculated strength recovery ratio remained above 95% for both aerogels (Figs. 11c, d and Table S1), demonstrating exceptional fatigue resistance.

Both materials exhibited strength recovery rates >95% upon stress release (Figs. 11c, d). Creep tests under 1 kPa stress (Figs. 11e, f) showed rapid deformation to stable strains at 25 °C, 50 °C, and 100 °C with no discernible creep over 1 hour. Elastic strains were 0.75%, 1.39%, and 1.88% for NC/$BiVO_4$-40@ $Ni_{0.95}Zn_{0.05}(OH)_{2.0}$ and 2.37%, 3.44%, and 3.68% for NC/$BiVO_4$-10@ $Ni_{0.95}Zn_{0.05}(OH)_{2.0}$ at the respective temperatures; complete recovery with zero residual strain confirmed structural stability across this range. Collectively, these results demonstrate the materials' capability to withstand repeated reactor operations and fluid dynamics in practical applications.

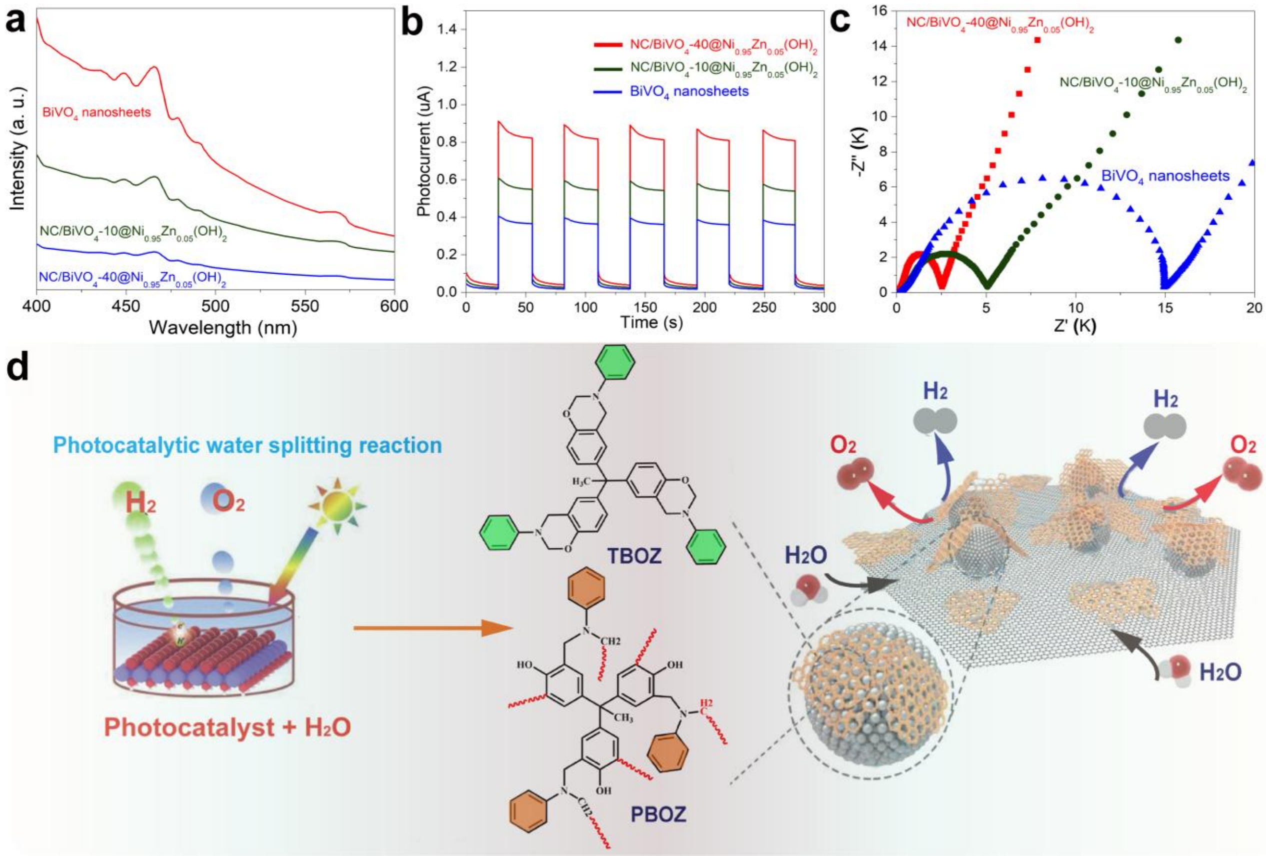

Fig. 12: Suppressed carrier recombination and enhanced charge separation efficiency. (a) PL spectra, (b) EIS Nyquist plots and (c) transient photocurrent responses of the NC/$BiVO_4$-10@$Ni_{0.95}Zn_{0.05}(OH)_{2.0}$, NC/$BiVO_4$-40@@$Ni_{0.95}Zn_{0.05}(OH)_{2.0}$ aerogels and the pristine $BiVO_4$ nanosheets; (d) Schematic illustrations of the charge transfer, separation and reaction of NC/$BiVO_4$ aerogels.

PL spectra can be employed to evaluate the photo-induced carriers trapping and recombination efficiency in the NC/$BiVO_4$-10@$Ni_{0.95}Zn_{0.05}(OH)_{2.0}$ and NC/$BiVO_4$-40@$Ni_{0.95}Zn_{0.05}(OH)_{2.0}$ aerogels, as well as the pristine $BiVO_4$ nanosheets (Fig. 12a). A wide PL speak was observed ranging from 400 to 480 nm for the pristine $BiVO_4$ nanosheets.[36] Nevertheless, the intensity of PL signal over the NC/$BiVO_4$-10@$Ni_{0.95}Zn_{0.05}(OH)_{2.0}$ and NC/$BiVO_4$-40@$Ni_{0.95}Zn_{0.05}(OH)_{2.0}$ aerogels dramatically decreased, which indicated that the separation efficiency of the photo-induced carriers (electrons and holes) was significantly enhanced, especially the NC/$BiVO_4$-40@$Ni_{0.95}Zn_{0.05}(OH)_{2.0}$ aerogel. The smallest semicircle in the EIS Nyquist plot of the NC/$BiVO_4$-40@$Ni_{0.95}Zn_{0.05}(OH)_{2.0}$ aerogel among the samples further verified this point (Fig. 12b). Generally, a smaller semicircle indicated that there was a faster interfacial electron transfer in the NC/$BiVO_4$ aerogels, contributing to a more effective separation of the photo-induced electrons and holes. The photocurrent-time curves of the NC/$BiVO_4$-10@$Ni_{0.95}Zn_{0.05}(OH)_{2.0}$ and NC/$BiVO_4$-40@$Ni_{0.95}Zn_{0.05}(OH)_{2.0}$ aerogels, as well as the pristine $BiVO_4$ nanosheets were shown in Fig. 12c. It can be seen that the photocatalysts maintain photostability after 120 s of photoelectrochemical tests and achieve the photocurrent densities of 0.87, 0.58 and 0.41 mA cm^{-2} for NC/$BiVO_4$-40@$Ni_{0.95}Zn_{0.05}(OH)_{2.0}$, NC/$BiVO_4$-10@$Ni_{0.95}Zn_{0.05}(OH)_{2.0}$ and the pristine $BiVO_4$ nanosheets, respectively, owing to the anchoring of an optimal ratio of the nitrogen self-doped carbon aerogels in the layered structure of $BiVO_4$ nanosheets.

As shown in Fig. 12d, the introduction of $BiVO_4$ nanosheets into the pores of carbon aerogels increased the structural disorder of the hybrids, which governed the photocatalytic reactivity, with more disordered carbons with smaller ordered domains exhibiting greater adsorption for -OH^- ions, leading to higher yields of H_2 and O_2. Irradiated by the visible light, the e^- in the VB of $BiVO_4$ was excited into the CB, while the h^+ was left behind in its VB. As an e^- acceptor, NC would accept the e^- from the VB of $BiVO_4$. The transferred e^- would participate in the water reduction reaction. Besides, water reduction reaction occurred under the trigger of the migrated h^+ on the surface of $BiVO_4$, leading to the generation of O_2 and H_2O_2. There is no doubt that the excellent photocatalytic performance of overall water splitting reaction for the NC/$BiVO_4$ aerogels cannot be divorced from the effective transfer and separation of e^- and h^+, owing to their particular geometric construction and strong adsorption capacity for -OH^- ions.

4. Conclusion

In summary, a range of phenolic resin derived hierarchical porous monolithic aerogels was constructed at a large scale based on the ring-opening polymerization of a branched benzoxazine monomer, in which few-layer $BiVO_4$ nanosheets was embedded with nitrogen self-doped carbon aerogels (NC). The resulting NC/$BiVO_4$ aerogels had macro-, meso-, as well as micropores, and high specific surface area (758.54-929.21 m^2 g^{-1}). The intrinsic electronic and band structure of NC/$BiVO_4$ aerogels can be tuned by the polymerization of three functional benzoxazine monomer and the gelation of polybenzoxazine in DMF. The optimized 3D NC/$BiVO_4$-40@$Ni_{0.95}Zn_{0.05}(OH)_{2.0}$ monolithic aerogel exhibited the highest photocatalytic H_2 evolution capacity (230.41μmol g^{-1} h^{-1}) via a two-electron pathway, which was 65 times higher than that of the pristine $BiVO_4$(3.55 μmol g^{-1} h^{-1}). Based on the as-synthesized electrode active species, we successfully assembled solar cells incorporating 3D monolithic NC/$BiVO_4$ aerogels decorated Ni-Zn batteries with a stable output voltage of 1.89 V. The solar-charged rechargeable Ni-Zn battery could run not only during the day but also at night, leading to a 24 h well-run fully solar-powered uninterrupted overall water-splitting system. We believe that using such uninterrupted solar-to-hydrogen conversion and storage systems could provide important opportunities for the development and application of renewable energy, which will accelerate the sustainable development of green energy management.

Acknowledgments

Financial support is acknowledged from the Anhui Provincial Key Laboratory of Green Carbon Chemistry, Key Program for Anhui Provincial Key Laboratory of Green Carbon Chemistry (AHGC2025013) and the Natural Science Research Projects of the Anhui Educational Committee (2024AH051470, 2024AH051454, and 2024AH051450), the Scientific Research Foundation of Fuyang Normal University (2023KYQD0074 and 2024KYQD0008), the College Students' Innovation and Entrepreneurship Training Program Projects (202410371005 and 202410371006), and the Key Project of the Youth Talent Fund of Fuyang Normal University.

Conflict of Interest

The author has no conflicts of interest to declare.

Supporting Information

Not applicable.

CRediT Statement

Ruhua Zha: Conceptualization, Methodology, Investigation, Writing - Original Draft. **Zhen Zhang:** Validation, Formal analysis, Visualization. **Yang Zhang:** Resources, Data curation. **QingCheng Wang:** Supervision, Project administration, Funding acquisition. **Liu He:** Investigation, Software. **Tuo Shi:** Writing - Review and editing, Supervision. **Min Zhang:** Conceptualization, Writing - Review and editing, Supervision.

References

[1] M. Stangalini, Wave energy in the solar atmosphere, *Nature Astronomy*, 2023, **7**, 761-762, doi: 10.1038/s41550-023-01955-5.

[2] F. J. M. M. Nijsse, J.-F. Mercure, N. Ameli, F. Larosa, S.

Kothari, J. Rickman, P. Vercoulen, H. Pollitt, The momentum of the solar energy transition, *Nature Communications*, 2023, **14**, 6542, doi: 10.1038/s41467-023-41971-7.

[3] Z. Wang, H. Hölzel, L. Fernandez, A. S. Aslam, P. Baronas, J. Orrego-Hernández, S. Ghasemi, M. Campoy-Quiles, K. Moth-Poulsen, Hybrid solar energy device for simultaneous electric power generation and molecular solar thermal energy storage, *Joule*, 2024, **8**, 2607-2622, doi: 10.1016/j.joule.2024.06.012.

[4] T. S. Horbury, T. Woolley, R. Laker, L. Matteini, J. Eastwood, S. D. Bale, R. Livi, Sharp Alfvénic impulses in the near-Sun solar wind, *The Astrophysical Journal Supplement Series*, 2020, **246**, 45-49, doi:10.3847/1538-4365/ab5b15.

[5] F. Zhao, C. Li, S. Li, B. Wang, B. Huang, K. Hu, L. Liu, W. W. Yu, H. Li, Continuous solar energy conversion windows integrating zinc anode-based electrochromic device and IoT system, *Advanced Materials*, 2024, **36**, 2405035, doi: 10.1002/adma.202405035.

[6] H. Pan, J. Li, Y. Wang, Q. Xia, L. Qiu, B. Zhou, Solar-driven biomass reforming for hydrogen generation: principles, advances, and challenges, *Advanced Science*, 2024, **11**, 2402651, doi: 10.1002/advs.202402651.

[7] A. Katepalli, Y. Wang, D. Shi, Solar harvesting through multiple semi-transparent cadmium telluride solar panels for collective energy generation, *Solar Energy*, 2023, **264**, 112047, doi: 10.1016/j.solener.2023.112047.

[8] Z. Xing, F. Liu, J. Feng, L. Yu, Z. Wu, B. Zhao, B. Chen, H. Ping, Y. Xu, A. Liu, Y. Zhao, C. Wang, B. Wang, X. Huang, Synergistic photobiocatalysis for enantioselective triple-radical sorting, *Nature*, 2025, **637**, 1118-1123, doi: 10.1038/s41586-024-08399-5.

[9] H. Zhang, J.-X. Chen, J.-P. Qu, Y.-B. Kang, Photocatalytic low-temperature defluorination of PFASs, *Nature*, 2024, **635**, 610-617, doi: 10.1038/s41586-024-08179-1.

[10] Z. Lian, Y. Kobayashi, J. J. M. Vequizo, C. S. K. Ranasinghe, A. Yamakata, T. Nagai, K. Kimoto, K. Kobayashi, K. Tanaka, T. Teranishi, M. Sakamoto, Harnessing infrared solar energy with plasmonic energy upconversion, *Nature Sustainability*, 2022, **5**, 1092-1099, doi: 10.1038/s41893-022-00975-9.

[11] Y. Xiao, X. Li, T. Zheng, K. Xiao, Y. Wang, Photothermal nanoreactors for photocatalytic solar energy conversion, *Coordination Chemistry Reviews*, 2024, **517**, 216017, doi: 10.1016/j.ccr.2024.216017.

[12] T. He, Y. Zhao, D. Benetti, B. Moss, L. Tian, S. Selim, R. Li, F. Fan, Q. Li, X. Wang, C. Li, J. R. Durrant, Facet-engineered $BiVO_4$ photocatalysts for water oxidation: lifetime gain versus energetic loss, *Journal of the American Chemical Society*, 2024, **146**, 27080-27089, doi: 10.1021/jacs.4c09219.

[13] L. Liu, M. Ruan, C. Wang, Z. Liu, Optimization of the BiO8 polar group of BiVO4 by Cl: embedded modification to manipulate bulk-surface carrier separation for achieving efficient piezo-PEC water oxidation, *Applied Catalysis B: Environment and Energy*, 2024, **354**, 124117, doi: 10.1016/j.apcatb.2024.124117.

[14] J. Zhang, X. Wei, J. Zhao, Y. Zhang, L. Wang, J. Huang, H. She, Q. Wang, Electronegative Cl – modified BiVO4 photoanode synergized with nickel hydroxide cocatalyst for high-performance photoelectrochemical water splitting, *Chemical Engineering Journal*, 2023, **454**, 140081, doi: 10.1016/j.cej.2022.140081.

[15] P. Wen, R. Lei, X. Cao, Q. Ma, G. Zhang, C. Guo, X. Wang, Y. Qiu, Anchored Ni nanocrystals boosting BiVO4 photoanode for highly efficient water oxidation *via in situ* generation of Ni@NiOOH co-catalyst, *Chemical Engineering Journal*, 2023, **454**, 139983, doi: 10.1016/j.cej.2022.139983.

[16] Y. Deng, J. Wang, J. Wang, W. Wang, H. Zhang, S. Yin, Restricted template – induced growth of vanadium oxide clusters on BiVO4 (1 1 0) crystal planes for an efficient catalytic conversion of CO_2 to methanol, *Chemical Engineering Journal*, 2024, **496**, 153963, doi: 10.1016/j.cej.2024.153963.

[17] S. Daemi, A. Kundmann, K. Becker, P. Cendula, F. E. Osterloh, Contactless measurement of the photovoltage in $BiVO_4$ photoelectrodes, *Energy & Environmental Science*, 2023, **16**, 4530-4538, doi: 10.1039/d3ee02087h.

[18] K. J. Wong, J. J. Foo, T. J. Siang, W.-J. Ong, Shining light on carbon aerogel photocatalysts: unlocking the potentials in the quest for revolutionizing solar-to-chemical conversion and environmental remediation, *Advanced Functional Materials*, 2023, **33**, 2306014, doi: 10.1002/adfm.202306014.

[19] N. Meng, Y. Zhang, W. Liu, Q. Chen, N. Soykeabkaew, Y. Liao, Monolithic conjugated microporous polymer aerogel for triboelectric nanogenerator, *Advanced Functional Materials*, 2024, **34**, 2313534, doi: 10.1002/adfm.202313534.

[20] Y. Wang, H. He, Y. Li, W. Wang, L. Deng, L. Wu, Y. Zhang, J. Huang, P. Zhang, G. Yu, Y.-N. Liu, Unraveling the photo-induced dynamic behavior of COF-based Z-scheme heterostructure monolithic aerogels, *Matter*, 2024, **7**, 3145-3162, doi: 10.1016/j.matt.2024.05.003.

[21] Y. Su, G. Yuan, J. Hu, G. Zhang, Y. Tang, Y. Chen, Y. Tian, S. Wang, M. Shakouri, H. Pang, Thiosalicylic-acid-mediated coordination structure of nickel center *via* thermodynamic modulation for aqueous Ni – Zn batteries, *Advanced Materials*, 2024, **36**, 2406094, doi: 10.1002/adma.202406094.

[22] F. Zhang, B. He, Y. Xin, T. Zhu, Y. Zhang, S. Wang, W. Li, Y. Yang, H. Tian, Emerging chemistry for wide-temperature sodium-ion batteries, *Chemical Reviews*, 2024, **124**, 4778-4821, doi: 10.1021/acs.chemrev.3c00728.

[23] Q. Chen, M. Lin, X. Li, Z. Du, Y. Liu, Y. Tang, Y. Yan, K. Zhu, Fabrication of azacrown ether-embedded covalent organic frameworks for enhanced cathode performance in aqueous Ni−Zn batteries, *Angewandte Chemie International Edition*, 2024, **63**, e202407575, doi: 10.1002/anie.202407575.

[24] M. Liang, Z. Li, Y. Kang, X. Zhao, X. Zhang, H. Zhang, H. Wang, Z. Miao, C. Fu, Ni_3S_2/Co_3S_4 with controlled surface electron arrangement for high-performance aqueous energy storage, *Journal of Materials Chemistry A*, 2024, **12**, 4623-4634, doi: 10.1039/d3ta06812a.

[25] Q. Zhang, X. Liu, Y. Lu, Y. Ni, W. Xie, Z. Yan, F. Li, J. Chen, Sustainable aqueous batteries based on bipolar dissociation of aluminum hydroxyacetate electrolyte, *Journal of the American Chemical Society*, 2024, **146**, 5597-5604, doi: 10.1021/jacs.3c13963.

[26] M. Zhang, M. Chen, N. Reddeppa, D. Xu, Q. Jing, R. Zha, Nitrogen self-doped carbon aerogels derived from trifunctional benzoxazine monomers as ultralight supercapacitor electrodes, *Nanoscale*, 2018, **10**, 6549-6557, doi: 10.1039/c8nr00207j.

[27] E. K. Goharshadi, A review on the radial distribution function: Insights into molecular structure, intermolecular interactions, and thermodynamic properties, *Journal of Molecular Liquids*, 2025, **433**, 127900, doi: 10.1016/j.molliq.2025.127900.

[28] X. Chen, D. Chen, J. Yu, Q. Guo, G. Li, X. Meng, J. Feng, L. Yu, L. Dong, Investigation on electron transfer process of oxygen reduction reactions catalyzed by nitrogen-doped graphitic carbon in acidic and alkaline media, *Journal of the Electrochemical Society*, 2021, **168**, 096508, doi: 10.1149/1945-7111/ac253f.

[29] M. Zhang, L. He, T. Shi, R. Zha, Neat 3D C_3N_4 monolithic aerogels embedded with carbon aerogels *via* ring-opening polymerization with high photoreactivity, *Applied Catalysis B: Environmental*, 2020, **266**, 118652, doi: 10.1016/j.apcatb.2020.118652.

[30] P. Hao, Z. Zhao, Y. Leng, J. Tian, Y. Sang, R. I. Boughton, C. P. Wong, H. Liu, B. Yang, Graphene-based nitrogen self-doped hierarchical porous carbon aerogels derived from chitosan for high performance supercapacitors, *Nano Energy*, 2015, **15**, 9-23, doi: 10.1016/j.nanoen.2015.02.035.

[31] X. Liu, Y. Liu, T. Liu, Y. Jia, H. Deng, W. Wang, F. Zhang, Alkali-mediated dissolution-recrystallization strategy for *in situ* construction of a BiVO4/$Bi_{25}VO_{40}$ heterojunction with promoted interfacial charge transfer: Formation mechanism and photocatalytic tetracycline degradation studies, *Chemical Engineering Journal*, 2022, **431**, 134181, doi: 10.1016/j.cej.2021.134181.

[32] Y. Liu, Q. Tian, S. Wang, Z. Li, X. Duan, L. Que, C. Pei, Preparation of boron carbide nanosheets with high neutron-shielding properties based on reduced graphene oxide aerogel, *Ceramics International*, 2020, **46**, 18131-18141, doi: 10.1016/j.ceramint.2020.04.134.

[33] S. Sriwichai, S. Sakulsermsuk, K. Wetchakun, P. Kidkhunthod, N. Wetchakun, Promotion of single-phase tetragonal BiVO4 by Y doping for improving photocatalytic activities, *Ceramics International*, 2025, **51**, 48146-48160, doi: 10.1016/j.ceramint.2025.08.073.

[34] L. Huangfu, S. Zhao, J. Li, Z. Yao, C. Li, S. Gao, J. Yu, The effect of SO_2 on the structural evolution of a supported $Mn_2V_2O_7$ catalyst and its $DeNO_x$ performance, *Catalysis Science & Technology*, 2021, **11**, 5598-5605, doi: 10.1039/d1cy00693b.

[35] A. C. Forse, J. M. Griffin, C. Merlet, P. M. Bayley, H. Wang, P. Simon, C. P. Grey, NMR study of ion dynamics and charge storage in ionic liquid supercapacitors, *Journal of the American Chemical Society*, 2015, **137**, 7231-7242, doi: 10.1021/jacs.5b03958.

[36] D. Dai, X. Liang, B. Zhang, Y. Wang, Q. Wu, X. Bao, Z. Wang, Z. Zheng, H. Cheng, Y. Dai, B. Huang, P. Wang, Strain adjustment realizes the photocatalytic overall water splitting on tetragonal zircon BiVO4, *Advanced Science*, 2022, **9**, 2105299, doi: 10.1002/advs.202105299.

Open Access